3D magnetic resonance velocimetry for the characterization of hydrodynamics in microdevices

Feryal Guerroudj, Laouès Guendouz, Rainier Hreiz, Jean-Marc Commenge, Jérémy Bianchin, Christophe Morlot, Tien Dung Le, Jean-Christophe Perrin

3D Magnetic resonance velocimetry for the characterization of hydrodynamics in microdevices: application to micromixers and comparison with CFD simulations

Feryal Guerroudj[1], Laouès Guendouz[1], Rainier Hreiz[2], Jean-Marc Commenge[2], Jérémy Bianchin[1], Christophe Morlot[3], Tien Dung Le[1] and Jean-Christophe Perrin[1*]

[*] to whom correspondence should be addressed: jean-christophe.perrin@univ-lorraine.fr

[1] Université de Lorraine, CNRS, LEMTA, F-54000 Nancy, France

[2] Université de Lorraine, CNRS, LRGP, F-54000 Nancy, France

[3] Univ Lorraine, CNRS, GeoRessources Lab, Blvd Aiguillettes, BP 70239, F-54506 Vandoeuvre Les Nancy, France

Highlights

- An NMR instrumentation is developed to measure 3D velocity fields in microdevices
- MRI measurements in an arrow-type micromixer are compared to CFD simulations
- Small manufacturing defects strongly affect the flow and the mixing performance
- Good agreement is obtained between numerical data and experimental measurements

Abstract

3D velocity field measurements in an arrow-type micromixer are performed using nuclear magnetic resonance (NMR) imaging methods. A specific device has been set up including a home-made radiofrequency milli-coil matching the geometry of the manufactured micromixer, allowing an improvement of the signal-to-noise ratio by a factor 7 comparing to a standard commercial hardware. The NMR images obtained are compared to computational fluid dynamics (CFD) simulations. The very good agreement obtained between numerical data and experimental measurements revealed, on the one hand, the capacity of the developed method to perform a detailed and accurate study of phenomena occurring in a microstructured system and on the other hand, the great impact of small manufacturing defects on the hydrodynamics in a micromixer and thus on the mixing performances.

Keywords: computational fluid dynamics, magnetic resonance imaging, micromixers, magnetic resonance velocimetry, NMR instrumentation

1. Introduction

Microstructured reactors are attracting a lot of interest due to their intense heat and mass transfer capabilities. Their potential has been demonstrated through many applications in chemistry and process engineering, for example for flexible and decentralized synthesis processes (Hessel et al., 2005; Lee & Fu, 2018). They allow fine control of selectivity in complex competitive syntheses, and thus a reduction in purification costs and energetic impacts. The growing interest in these microstructured systems has led to more and more innovative designs and a variety of different geometries are presented in the literature from simple to complex (Bayareh et al., 2020). In the case of micromixers, a simple design (T or Y shape) can be as efficient as a more complex one (Dreher et al., 2009), the mixing performance being essentially related to the amount of mechanical energy injected and whether it is injected at the precise location where it is needed (Falk & Commenge, 2010). The studies carried out on micromixers with the T and Y geometries showed that in a range of Reynolds numbers between $Re = 5$ and $Re = 600$, several hydrodynamic regimes govern the flow in the mixing channel and impact the mixing quality (Engler et al., 2004; Galletti et al., 2019; Hsieh, 2013; Lobasov et al., 2018; Peng et al., 2022). With a high sensitivity to the local geometry (channel angle and cross section), with increasing Reynolds number values, the so-called stratified flow first evolves to a steady symmetric vortex flow, which becomes asymmetric, then periodic and finally unsteady, before reaching the laminar-turbulent transition around $Re = 600$. These flow regimes drastically improve the mixing quality and thus manage to reconcile performance and manufacturing simplicity. Experimental quantification of the mixing efficiency of micro-mixers is mainly performed via chemical characterizations using selective test reactions, such as the Villermaux-Dushman protocol, in which information on the mixing performance is given by the spectrophotometric analysis of the reaction products (Commenge & Falk, 2011). Other

experimental methods use optical detection, which is generally the method of choice to study microfluidic devices. Optical methods are however limited to transparent media and might be either invasive as they usually require the use of tracers that can alter the properties of the fluid system, or unconclusive as soon as vortical multilamination effects alter the contrast in the field of view. Additional information on the evolution of the flow regime in micromixers can be obtained by means of analytical methods or numerical simulations, but the latter are generally performed in ideal geometries i.e. without considering potential imperfections such as geometric defects that may result from the fabrication of these microscale systems.

Experimental methods based on the nuclear magnetic resonance (NMR) phenomenon allow non-invasive analysis of flows in microdevices. In literature NMR is conventionally used as a powerful analytical method in chemistry (Ionin & Ershov, 1995), biology (Wüthrich, 1990), rheology (Milc et al., 2022), porous media (Ferrari et al., 2018; Perrin et al., 2022), materials (Blümich Bernhard, 2000; Robert et al. 2018), in the biomedical field (Pettegrew, 2012) or in medicine through magnetic resonance imaging (MRI). Although existent, the literature on the application of MRI tool for the characterization of hydrodynamics (Gladden & Alexander, 1996; Stapf & Han, 2006) and compared to CFD simulations in engineering is sparser (Mendez et al., 2017; Chung et al. 1993). Indeed, NMR gives access to quantitative 3D measurements of the flow field, including in opaque devices that are inaccessible to optical velocimetry techniques. Moreover, its time-resolution is sufficient for characterizing transient flow phenomena (Callaghan & Xia, 1991; Oliveira et al., 2020; Seymour & Callaghan, 1997).

In practice, limitations related to measurement sensitivity may preclude the use of NMR on small scale devices handling a very low fluid volume when using standard methods and commercial hardware. Significant progress has been made over the last years in the NMR characterization of

such small systems (down to the nanoliter) (Lacey et al., 1999; Webb, 2012) by increasing the strength of the static magnetic field (Fu et al., 2005) or by using cryoprobes (Kovacs et al., 2005). Another efficient approach to improve the signal-to-noise ratio and allow direct access to the internal parts of the microstructured device is to reduce the dimensions of the radio frequency (RF) coil in order to cover the region of interest as closely as possible and thus maximize the so-called filling factor, *i.e.* the fraction between the sample volume and the coil volume (Hoult & Richards, 2011; Webb, 2008, 2013). Specific three-dimensional or planar (two-dimensional) coils have been designed for small volume samples (Eroglu et al., 2003; Massin et al., 2002; Olson et al., 1995; Peck et al., 1995; Trumbull et al., 2000) using specific microfabrication techniques such as laser processing or etching and copper printing (Klein et al., 2013a) or deposition on supports such as polyimide films (Dechow et al., 2000; Meier et al., 2014; Murphree et al., 2007; Woytasik et al., 2006). These types of coils are incorporated into microstructured devices for microscale studies such as quantitative reaction monitoring of processes (Ciobanu et al., 2003; Wensink et al., 2005), dynamic studies in devices handling small volumes (Harel & Pines, 2008; Klein et al., 2013b; J. Zhang & Balcom, 2010; X. Zhang & Webb, 2005) or performing velocity field mapping and distributions inside micromixers (Ahola et al., 2006, 2012; Akpa et al., 2007).

In this study, an NMR instrumentation is specifically developed for 3D velocity field measurements in a micromixer of millimeter dimensions. The MRI results obtained are compared to computational fluid dynamics (CFD) simulations to study the hydrodynamics in the device highlighting the sensitivity of the flow and mixing performances to the presence of small manufacturing defects.

2. Materials and Methods

2.1. Conception, fabrication and characterization of the micromixer

The micromixer investigated in this study has been machined in a block of polymethyl methacrylate (PMMA) using a digital milling machine. It consists of three cylindrical channels, with an internal diameter of 1 mm, arranged in an arrow configuration (Figure 1). The mixing angle, $\theta = 30°$, defines the angle between the axes of the outlet and one inlet. The zone of confluence of the three channels will be referred throughout this paper as “mixing zone”, and the point where their axes are supposed to meet will be referred as "mixing point”.

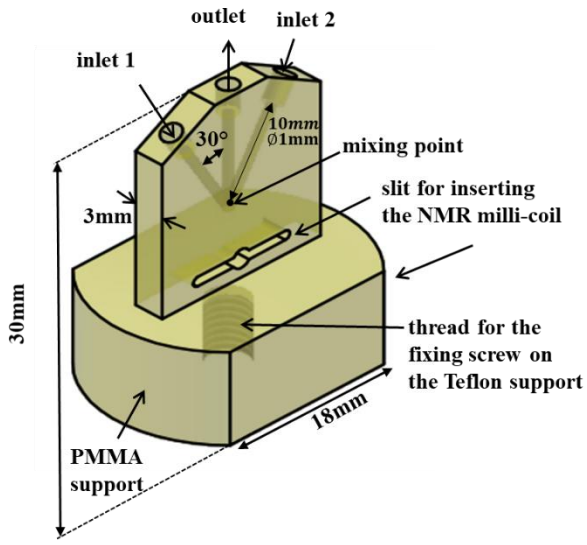

(a)

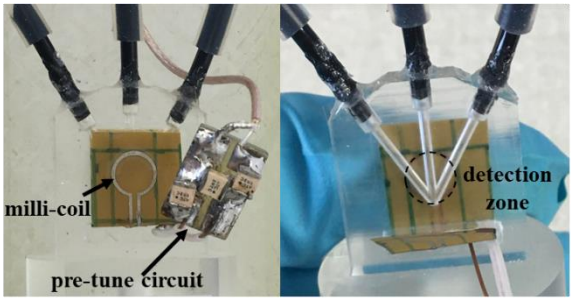

(b)

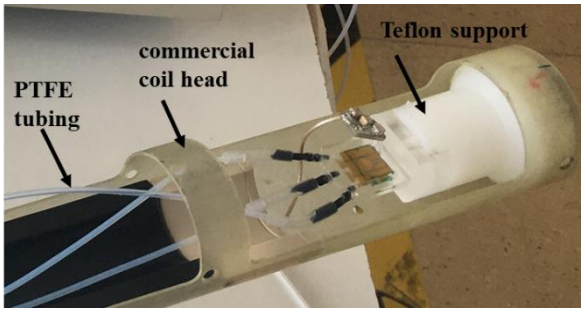

(c)

Figure 1: Experimental setup. (a) Schematic description of the fabricated micromixer. (b) Front view showing the NMR coil folded on both sides of the detection zone. (c) Assembly mounted on a commercial coil head ready to be inserted into the spectrometer.

113

114 As discussed later in this paper, large differences were observed between the experimental
115 velocity measurements and the first CFD simulations, which raised doubts about the presence of
116 manufacturing defects in the prototype. In order to check this possibility, 3D images of the

micromixer were recorded by MRI and X-ray Computed Tomography (µCT) for characterizing its true geometry. The MRI was performed on a Bruker Avance III 600 WB spectrometer. The superconducting magnet is oriented vertically and generates a static magnetic field B_0 with an intensity of $14.1\,\mathrm{T}$ which corresponds to a proton ^{1}H Larmor frequency of $600\,\mathrm{MHz}$. The spectrometer is equipped with a commercial Bruker MicWB40 microimaging coil. The micromixer was filled with a $CuSO_4$ solution $0.01\,\mathrm{M}$ in order to shorten the NMR relaxation time. The acquired image, consisting of voxels of $100 \times 100 \times 54\ \mu m^3$, provided a 3D mapping of the micromixer (see Fig.S1 of the Supporting information). The analysis of the obtained data revealed a slight misalignment of the three microchannels. Indeed, the two inlet axes and the outlet axis do not perfectly converge toward the supposed mixing point (Fig. S2). Moreover, the images analysis revealed the presence of two relatively large machining chips nearby the mixing zone, the first at the end of one inlet, and the second one at the entrance of the outlet channel (Figure 2 and Fig.S3).

A X-ray µCT scan was also performed in order to characterize the micromixer with a higher spatial resolution. The dataset was recorded using a Phoenix Nanotom $180\ kV$ GE X-ray system with a source-sample distance of $30\ mm$, an accelerating voltage of $80\ kV$ and a current of $80\ \mu A$. The spatial resolution was set to $6.81\ \mu m/voxel$. $2\,000$ projections were made (as averages of 3 projections of $1\,000\ ms$ each), resulting in a scan time of $134\ min$. Data processing was done using Avizo® 2022 and VGSstudio 3.5.

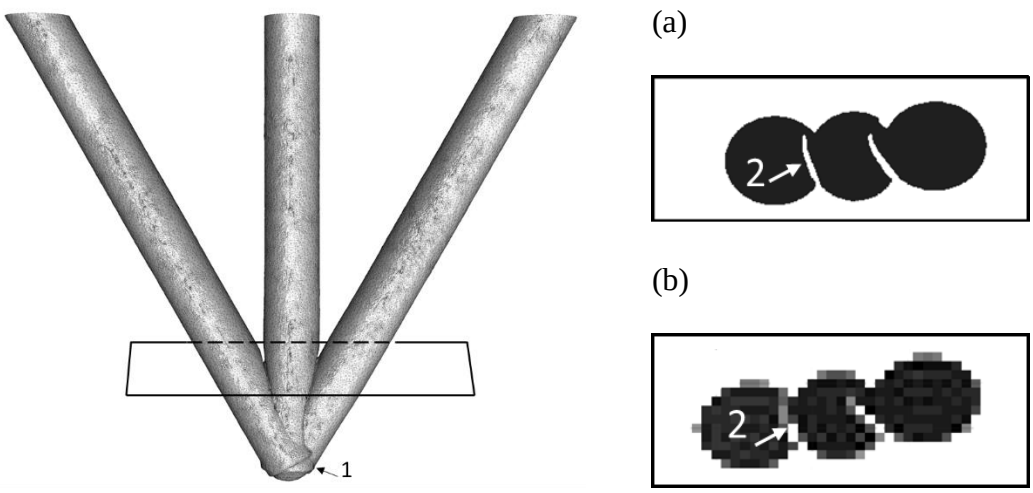

Figure 2: 3D image of the micromixer, obtained by X-ray µCT, showing manufacturing defects. (1): The black arrow shows a misalignment of the 3 channels. (2): Ortho-slice recorded near the mixing point: the white arrows show the presence of solid parts as observed by X-ray µCT (a) and MRI (b)

The raw images were segmented in order to isolate the three channels. The ortho-slice in the vicinity of the mixing point (Figure 2) confirmed the presence of the solid PMMA residues (white color, showed with the white arrows) that were not removed during the milling process. As discussed later in the results section, compared to the "ideal geometry" case, the presence of these defects leads to significant perturbations of the hydrodynamics in the micromixer.

2.2. MRI instrumentation and experiments

2.2.1. MR velocimetry measurements

MRI allows the localization of the ^{1}H NMR signal in order to reconstruct a 1D, 2D or 3D image. The principle relies on the application of consecutive magnetic field gradient pulses that make the main magnetic field B_0 vary along the three spatial directions and modifies the precession frequency of the proton ^{1}H nuclear magnetic moments according to Larmor's law (frequency encoding) as well as their phase (phase encoding). Details about the formation of MRI images are fund in textbooks (Callaghan, 1991). The schematic of the 2D velocimetry gradient-echo sequence used in this study is shown on Figure 3. In order to measure velocity components, a specific

encoding of the positions of the magnetic moments is produced by two gradient pulses of amplitude G_v, duration δ and separated by a time Δ (Caprihan & Fukushima, 1990; Callaghan, 1991; Blümich, 2000). The relationship linking the phase Φ of the measured NMR signal and velocity is given by the relation :

$$\Phi = \gamma \delta \Delta \overrightarrow{G_v}.\vec{v}$$

where γ is the proton gyromagnetic ratio.

In practice, a phase difference image is recorded, taking as reference the image measured when $G_v = 0$. Since the direction in which the flow is measured is determined by the direction of the encoding gradient, the velocity vector is determined at each position in a 2D section by applying $\overrightarrow{G_v}$ along the three orthogonal directions in space.

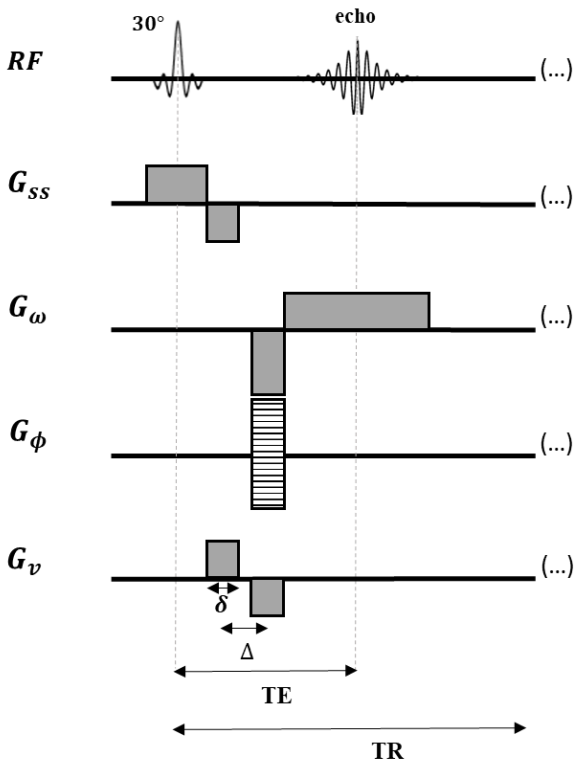

Figure 3: Acquisition protocol of 2D MRI velocity maps, based on the gradient echo sequence.

RF: radiofrequency pulses

G_{ss}: slice-selection gradient

G_ω: frequency-encoding gradient

G_ϕ: phase-encoding gradient

TE: echo time

TR: repetition time

G_v: velocity-encoding gradient

To perform the MR velocimetry experiments, the micromixer was integrated inside a home-made specific radiofrequency (RF) coil which was used for both the RF emission and the reception of the NMR signals. The assembly was placed in a gradient imaging system delivering a maximum magnetic field gradient intensity of $150\ G/cm$.

2.2.2. Specific MRI instrumentation

The developed radiofrequency milli-coil was adapted to the geometry and dimensions of the micromixer (Figure 1 (b) and Figure 1(c)). The geometry chosen for this study was a Helmholtz coil composed of a pair of copper loops placed face to face and $2.5\ mm$ apart. The diameter of each loop was $5\ mm$. The fabrication of the milli-coil was realized using an etching process on a DuPont™Pyralux®AC flexible copper/Kapton polyimide substrate. The width of the copper strip etched on the polyimide substrate was $0.4\ mm$ and its thickness was $45\ \mu m$. The fabricated milli-coil was connected to an electronic circuit composed of capacitors so that the resulting RLC circuit resonated at the proton (^{1}H) resonance frequency of $600\ MHz$ (tuning) and its impedance matched the characteristic impedance of the coaxial cable used for the transmission of the generated RF pulses and the received NMR signal (matching). For tuning and matching, a commercial exchangeable surface coil head Bruker MicWB40 was re-used. A pre-tuned circuit was added to complete the tuning with a set of fixed capacitors: ($C_{tuning} = 2.7\ pF, C_{matching} = 1.2\ pF$).

Electromagnetic simulations were carried out in order to determine the distribution of the radiofrequency field generated at $600\ MHz$ by the fabricated milli-coil. The simulations were performed with COMSOL multiphysics® and allowed computing the normalized radiofrequency field intensity over a $5.7\ mm$ distance in the direction of the outlet of the micromixer. The measurement of the NMR signal intensity map (Figure 4 (b)), performed on the micromixer filled with the copper sulfate solution is in very good agreement with this simulation (Figure 4 (c)).

According to these results, the profiles present a plateau where the radiofrequency field is homogeneous. The deviation from homogeneity over a length of 2 *mm* is only 1.3 % on the profile obtained by the electromagnetic simulation and 3 % on the MRI profile.

For a detailed and accurate study of the hydrodynamics occurring in the micromixer, the MRI velocity measurements presented in this work were located within the homogeneity zone of the radiofrequency field produced by the milli-coil.

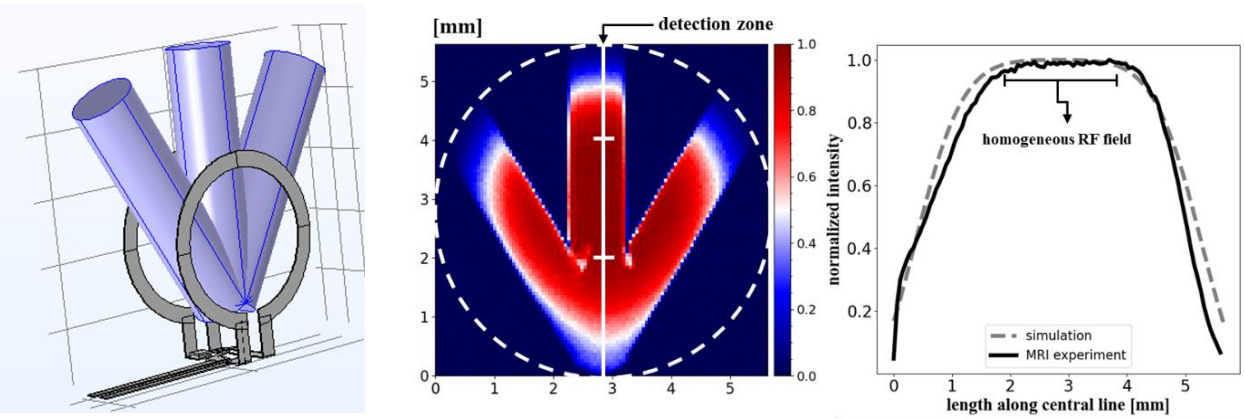

(a) (b) (c)

Figure 4: (a) Schematics of the Helmholtz NMR coil, composed of a pair of copper loops placed face to face on either side of the mixing zone. (b) Normalized 2D MR image of the $CuSO_4$ solution in the mixer. (c) Comparison of the experimental and simulated normalized NMR intensity profiles along the centerline of the outlet channel showing a homogeneous intensity plateau of about 2 mm in length.

In order to evaluate the improvement of the signal-to-noise ratio (SNR), MRI measurements were performed on both the milli-coil and the commercial coil Bruker MicWB40 (with a detection volume 10 times larger) in similar conditions.

An axial NMR signal intensity map (measured in the plane orthogonal to the main flow direction) was performed with the milli-coil considering a field of view of $7.5 \times 7.5\ mm^2$, corresponding to a spatial resolution of $30 \times 30\ \mu m^2$ per pixel. The NMR signal was averaged over a slice thickness of $200\ \mu m$ and accumulated 8 times. The slice position considered is at $3\ mm$ from the mixing point. A similar measurement was performed with the commercial coil Bruker MicWB40. The results demonstrate a ~ 7 fold improvement of the SNR, evaluated by dividing the mean value of the signal (in the channel) by the mean value of the noise (outside the channel). The improvement of the signal-to-noise ratio with the developed milli-coil allows, with a higher image quality, a detailed characterization of the velocity field in the micromixer (Figure 5).

(a)

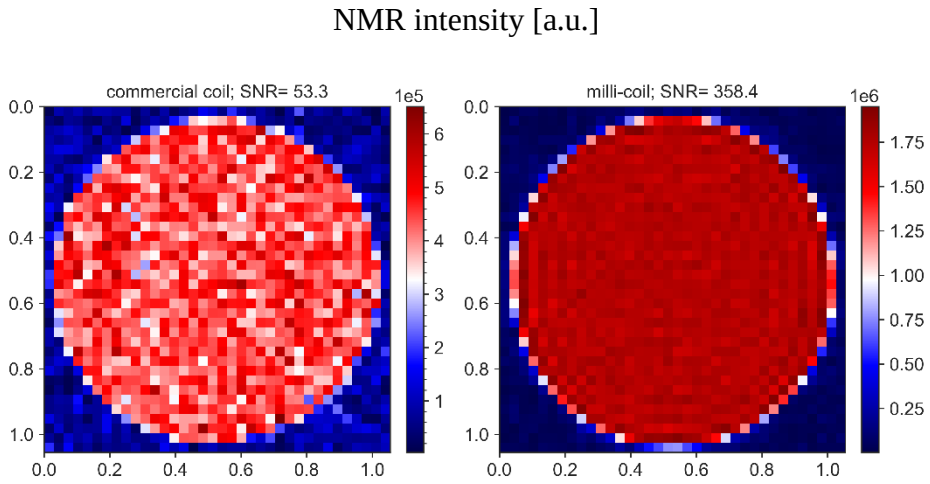

(b)

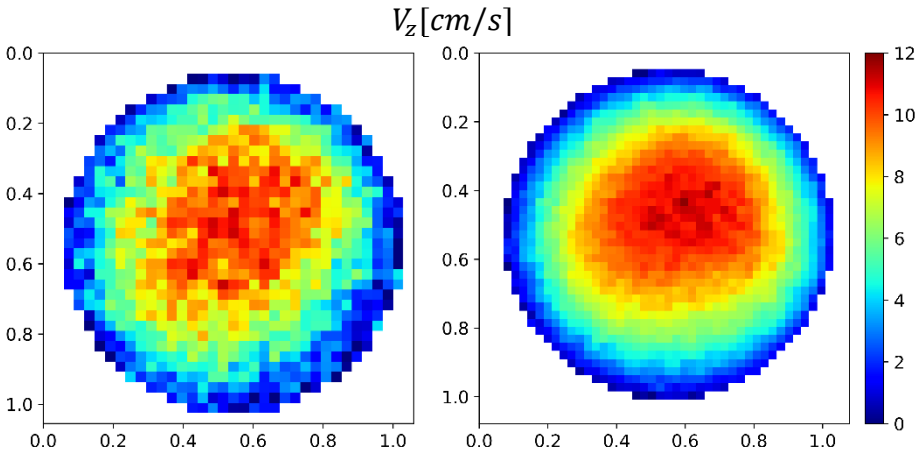

Figure 5: comparison of the MRI measurements performed with the commercial coil and with the milli-coil showing the improvement of the signal to noise ratio and the image quality. (a) 2D NMR signal intensity maps (b) 2D velocity map of the z component (flow rate $1.4\ ml/min$ *per inlet, slice thickness* $0.2\ mm$*, slice position at* $3\ mm$ *from the mixing point) obtained with the commercial coil Bruker MICW40 (*$25\ mm$ *ID), in-plane resolution* $30 \times 30\ \mu m^2$ *and* $8\ accumulations$ *of the NMR signal) and with the developed milli-coil (in-plane resolution* $24 \times 24\ \mu m^2$ *and* $4\ accumulations$*). The distances on the axes are in millimeters.*

204

205 *2.2.3. Parameters and conditions for MRI velocity measurements*

206 The fluid flowing through the micromixer was an aqueous $CuSO_4$ solution 0.01 M characterized
207 by a longitudinal relaxation time $T_1 \sim 100\ ms$. This concentration is adequate to significantly
208 shorten the NMR relaxation times while remaining sufficiently low to not alter the physical
209 properties of the water phase, including the self-diffusion coefficient. The water flow was achieved
210 through $1\ mm$ ID PTFE tubings using a multi-channel peristaltic pump (Ismatec Reglo ICC
211 Digital) used with Tygon® S3™ E-LFL, $1.52\ mm$ ID pump tubing. The peristaltic pump ensures
212 that a same flow rate was injected at each inlet during all the experiments. Experiments were
213 conducted for eight different flow rates ranging from 1.4 to 4.2 ml/min at each inlet (see Table
214 1), corresponding to outflow Reynolds numbers in the range $[59 - 178]$ (note that the outflow
215 Reynolds number is the double of that of the inflow).

216 The protocol described earlier (gradient echo sequence with phase encoding) was used to measure
217 both axial (in planes orthogonal to the main flow direction) and sagittal velocity maps (in a plane
218 orthogonal to the axial images containing all three channels of the micro-mixer). The measurements
219 were carried out using the parameters summarized in Table 2. Each velocity component was
220 mapped separately, the *z*-component corresponding to the main flow direction. In order to check

the accuracy of the measurements, the average flow rate was calculated from the velocity images in several sections and for the different flow rates supplied by the pump. The results agree over the entire measurement range, with an error of less than 5%. The reconstruction of the velocity field was made with Paravision 5.1 software. The presentation of the maps and the comparison with the CFD results were done using Python 3.7 in Jupyter Notebook 6.0.1.

Table 1: flow conditions in the micromixer

Flow rate per inlet ($\boldsymbol{ml/min}$)	Reynolds number (outflow)	Maximum velocity (Poiseuille flow) (cm/s)
$\mathbf{1.4}$	59	12
$\mathbf{1.9}$	80	16
$\mathbf{2.4}$	102	20
$\mathbf{2.9}$	123	25
$\mathbf{3.2}$	136	27
$\mathbf{3.4}$	144	28
$\mathbf{3.9}$	165	30
$\mathbf{4.2}$	178	32

Table 2: parameters for MRI velocity measurements

	Parameter	Characteristics
	TR	300 ms
	TE	5 ms
	Δ	2.16 ms
	δ	2.05 ms
	acquisition time	300 s
	accumulations	4
axial images	thickness	200 µm
	field of view	6×6 mm^2
	spatial resolution	24×24 µm^2
sagittal images	thickness	400 µm
	field of view	1×1 cm^2
	spatial resolution	39×39 µm^2

2.3. CFD modeling and simulation

2.3.1. Geometry and mesh

Modeling and CFD simulations of the hydrodynamics in the micromixer were conducted using the ANSYS 2019 commercial software package (including ANSYS Fluent). A first geometry was drawn using ANSYS Design Modeler following the dimensions presented in Figure 1 (a), i.e. a diameter of 1 mm with inlets and outlet pipes of 10 mm length each. This design will be referred through the remaining of this paper as "ideal geometry". ANSYS Meshing software was used for meshing the numerical domain. Given the form of the micromixer, the mixing zone was meshed using tetrahedral cells while the remaining parts, consisting of the inlets and outlet channels, were

discretized using hexahedral elements (Figure 6). A total of about 13.4×10^6 cells was employed for ensuring a mesh-independent solution for all the cases studied.

As discussed later in this paper, numerical results obtained using the "ideal geometry" did not allow reproducing the experimental velocity fields. Accordingly, as explained in Section 2.1, the real micromixer geometry has been identified through X-ray µCT scanning. This second design will be referred through the remaining of this article as "real geometry". As mentioned earlier and detailed in the Supplementary material section, compared to the "ideal geometry", the real one involves a slight misalignment of the inlets and outlet microchannels and includes two relatively large machining chips nearby the mixing zone. The "real geometry" was first meshed via Avizo software and then exported toward ANSYS Meshing where the mesh was further refined reaching a total of about 7.9×10^6 tetrahedral elements (Figure 6). Such a large number of computational cells is necessary for reaching mesh-independent solutions given the significant levels of numerical diffusion of tetrahedral elements.

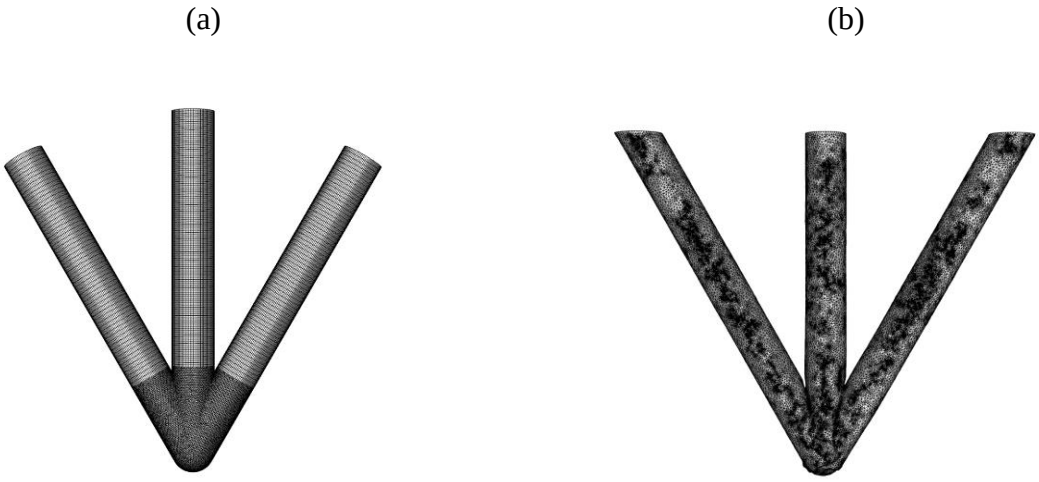

Figure 6: Mesh used for the CFD simulations corresponding to the "ideal geometry" (a) and the "real geometry" (b) of the micromixer.

2.3.2. Hydrodynamics modeling

For both ideal and real geometries, the flow field has been determined by solving the Navier-Stokes equations assuming an incompressible and isothermal flow (and hence, uniform water properties):

$$div(\vec{u}) = 0 \tag{1}$$

$$\rho \frac{\partial \vec{u}}{\partial t} + \rho \overrightarrow{div}(\vec{u} \otimes \vec{u}) = -\vec{\nabla} p^* + \mu \vec{\Delta} \vec{u} \tag{2}$$

where t denotes time, $\vec{u}$ the velocity vector, ρ the water density, μ its dynamic viscosity and p^* the driving pressure.

The first term in Equation 2 describes transient flow behavior. Since this study focuses on the steady-state regime only, this term has been considered null and a steady-state solver has been used to compute the steady-state solution. However, for the "real geometry" case under a flow rate of $4.2\ ml/min$ at each inlet, convergence could not be achieved this way. Indeed, under these operating conditions, the machining chips led to some low amplitude vortex shedding phenomena. Hence, for this case only, the full unsteady Navier-Stokes equations were solved until reaching the permanent flow regime where the time-averaged solution was computed. Advancement in time was achieved through a second-order implicit scheme with time steps of $10^{-4}s$.

Simulations were conducted considering uniform velocity profiles at the inlets, uniform pressure at the outlet and no-slip condition at the wall. The advective terms have been discretized using the QUICK scheme and the diffusion terms were central-differenced.

Since MRI measurements correspond to space-averaged (namely along the depth of the sample slices) velocities, in order to allow reliable comparison, CFD data were interpolated over a coarser

grid corresponding to the MRI slice thickness in order to achieve the same spatial resolution between experimental and numerical results (see Fig.S4).

2.3.3. CFD investigation of mixing efficiency

As detailed later in the results section, flow simulations revealed that manufacturing defects and the presence of residual machining chips have significant effects on the hydrodynamics in the micromixer, which is expected to substantially impact the mixing efficiency. Accordingly, mixing simulations were conducted using both the "ideal" and "real" geometries, and that for all of the 8 flow rates investigated in this study (

).

These simulations consist in continuously injecting a tracer (i.e. a passive scalar) at one inlet where its concentration is assumed to be uniform and equal to C_{max}, whereas at the second inlet, its concentration is considered to be zero, i.e. tracer-free water is injected. It should be underlined that the value of C_{max} is arbitrarily chosen as it does not influence the mixing quality. Indeed, the tracer concentration is assumed to have no effect on the water density or physiochemical properties.

The concentration field is determined by solving the mass transport equation:

$$\frac{\partial C}{\partial t} + div(C\,\vec{u}) = D\,\Delta C \qquad (3)$$

where *C* is the tracer local concentration and *D* its molecular diffusivity in the liquid, taken here as $2 \times 10^{-9}\, m^2\, s^{-1}$ which corresponds to water self-diffusion coefficient at $20\,°C$. At the outlet section, a zero normal-concentration-gradient boundary condition is assumed.

The first term in Equation 3 corresponds to temporal variations. As for the flow simulations (Section 2.3.2), it was considered null apart for the case involving the "real geometry" under a flow rate of 4.2 ml/min at each inlet where no steady-state solution could be achieved. For this case, Equations (1), (2) and (3) are simultaneously solved using a time step of $10^{-4}\ s$ until reaching the permanent flow regime where the time-averaged solution is computed.

Mixing quality can be quantified by computing the concentration standard deviation at the outlet or more correctly, the concentration mass-weighted uniformity index. However, because of the low diffusivities of liquids, when dealing with laminar or transitional flows as in this study, numerical diffusion effects become significant and may even exceed molecular diffusion effects. This is particularly true when the computational domain involves tetrahedral cells. Therefore, despite the large number of computational elements used (Section 2.3.1) which sufficiently reduces numerical diffusion, mixing simulations will be only qualitatively analyzed in this article. No quantification of the mixing quality will be presented so as to not cumbersome the paper with discussions on numerical diffusion effects especially since no experimental measurements are available for supporting mixing simulations results.

3. Results and discussion

3.1. *Hydrodynamics in the micromixer*

3.1.1. CFD simulations with the "ideal geometry"

CFD simulations carried out using the "ideal geometry" revealed similar flow behavior (presented in Figure 7 and Fig.S5 to Fig.S11 in the supplementary material) for all eight flow rates investigated (

312). The flow remains steady and preserves its double symmetry along the zy and zx planes. At
313 the entrance of the outlet channel (i.e., in the vicinity of the mixing zone), four vortices develop in
314 the cross-stream direction, and their intensity increases with increasing flow rate. Indeed, once
315 inertial effects are sufficient, secondary flow structures are known to form in the mixing channel
316 (Bothe et al., 2006; Lobasov et al., 2018). These vortices promote lateral displacement of the fluid
317 parcels and thus enhance the mixing quality. When progressing downstream toward the outlet, the
318 secondary flow intensity attenuates (and thus the cross-stream velocity components) as the flow
319 becomes increasingly axisymmetric and tends to fully develop into a classic Poiseuille profile. As
320 could be expected, the development length increases with the flow rate.

321 *3.1.2. MRI velocity measurements vs CFD results*

322 MRI velocity measurements along the outlet channel confirmed some of the general flow
323 features predicted by the CFD simulations with the "ideal geometry" (Section 3.1.1) such as the
324 presence of secondary flows. Nonetheless, major differences existed between experimental and
325 numerical results. Indeed, MRI revealed that even for the lowest flow rates investigated, the double
326 symmetry of the flow is not preserved (Figure 7 and Fig. S12 to Fig. S15 in the supplementary
327 material). The secondary flows consisted of one or two asymmetric cells rather than four vortices
328 as predicted by the simulations.

329 As discussed in Section 2.1, these large differences between numerical and experimental data
330 raised doubts about the presence of manufacturing defects in the prototype. Accordingly, the real
331 geometry of the micromixer was recorded using X-ray CT which revealed some minor defects as
332 well as the presence of two machining chips that were not removed during the milling process as
333 explained earlier.

CFD results obtained using the "real geometry" are in very good agreement with experimental measurements as can be seen in Figure 7 (and Fig. S16 to Fig. S22 in the supplementary material), and allow reproducing the high asymmetry of the velocity fields as revealed by the MRI, which proves that even small defects may have a big impact on the hydrodynamics and hence on the mixing efficiency in micromixers. We note that the velocity map presented on Figure 7a shows important phase wrapping in the mixing zone (V_x component), manifested by an abrupt change in velocity for small lateral displacements. We have not tried to correct this artifact because the axial maps discussed in this paper are measured well above the mixing zone.

For the lowest flow rate investigated, CFD results are in excellent agreement, qualitatively and quantitatively, with experimental data (Figure 8). As the flow rates is increased, although it remains acceptable, the agreement between the two sets of results tends to decrease, and this for different reasons. Indeed, with increasing flow rates, larger velocity gradients occur in the mixing zone, i.e. velocity values vary more and more significantly along the axial position along the outlet channel, in particular in the vicinity of the mixing zone. Accordingly, a small uncertainty in the exact location of the MRI measurement section may lead to large differences with the numerical results as the flow becomes very sensitive to axial position. Moreover, MRI images accuracy deteriorates as the velocities are gradually increased. For instance, from a flow rate of 3.9 ml/min at each inlet (corresponding to axial velocities in the mixing channel reaching about 30 cm/s, see Table 1), measurements using the current experimental apparatus are no longer reliable as the signal-to-noise ratio becomes very low (Fig. S23 in the supplementary material). The effect of temporal averaging during the observation time Δ should also be considered to better understand the limitations of the measurements. Indeed, when the flow rate is high, the average fluid displacement during Δ can be much larger than the voxel sizes which can lead to significant image distortions. This should be

taken into consideration for further comparison and to better delimit the range of velocities accessible to the experiment.

In any case, in the range of the measurable velocities, the successful comparison between MRI measurements and CFD data allows validating the presence of complex flow features in the mixing channels and reveals the great impact that small manufacturing defects may have on the hydrodynamics in micromixers.

(a)

CFD

ideal geometry

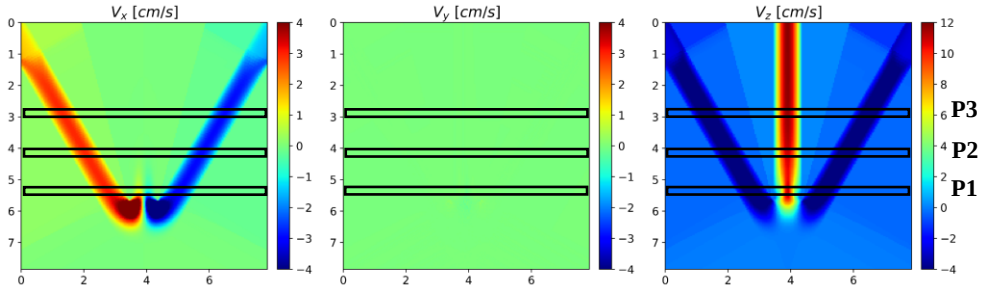

CFD

real geometry

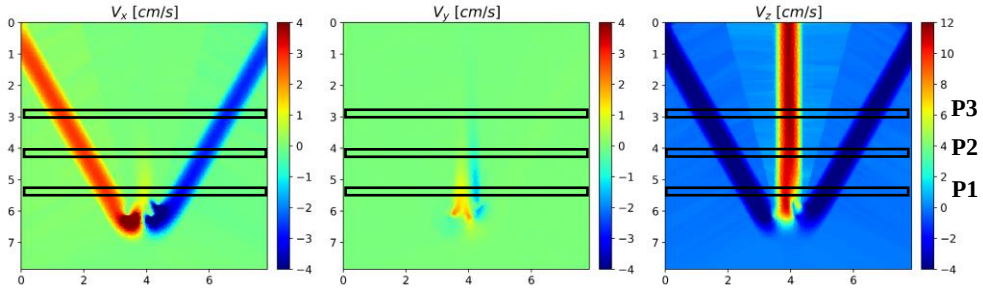

MRI

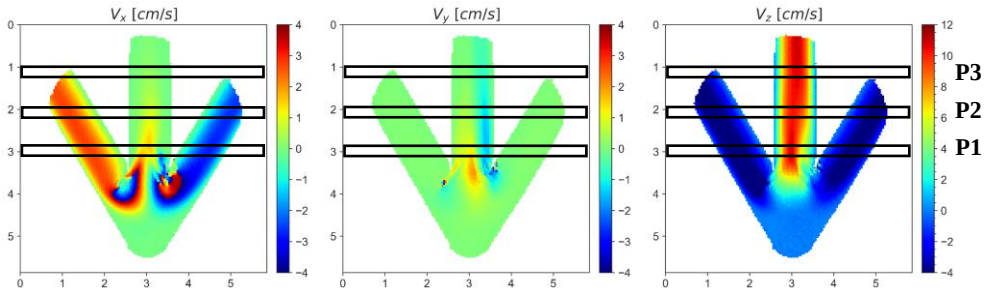

365

366

367

(b) slice position P1

CFD

ideal geometry

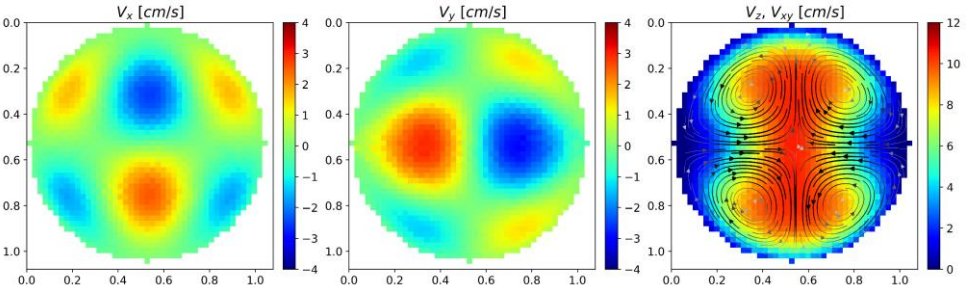

CFD

real geometry

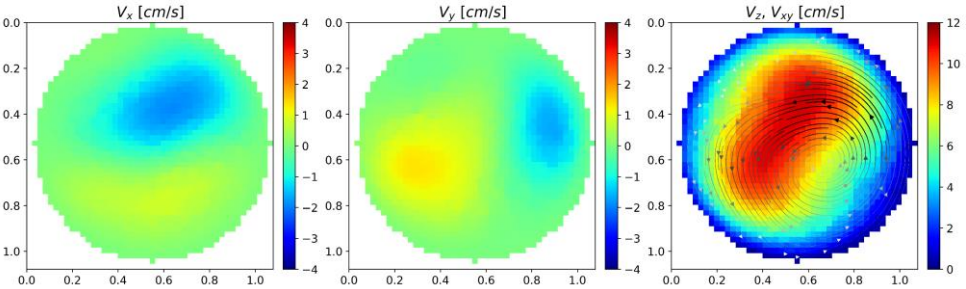

MRI

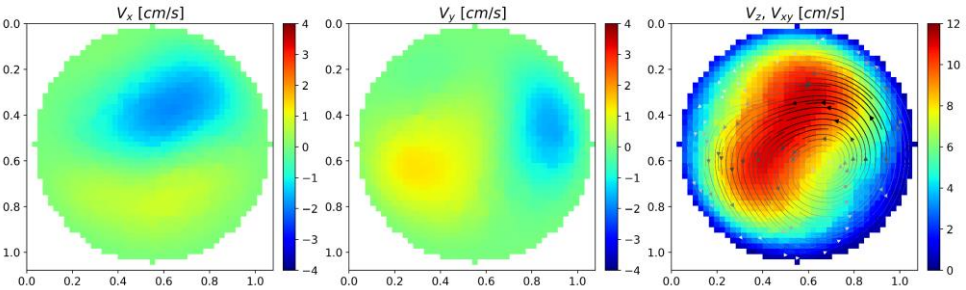

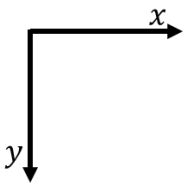

central profile

along x

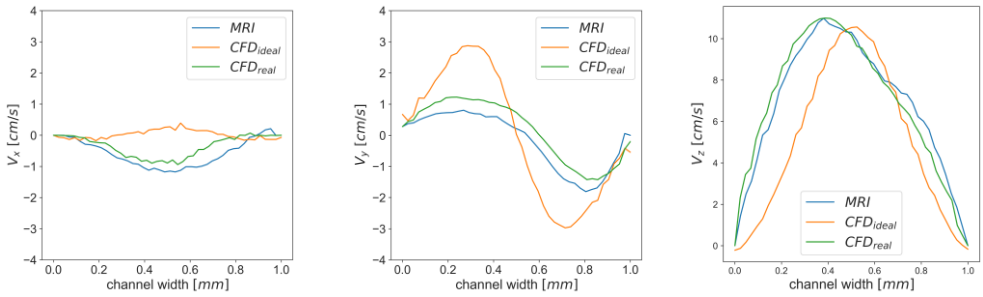

central profile

along y

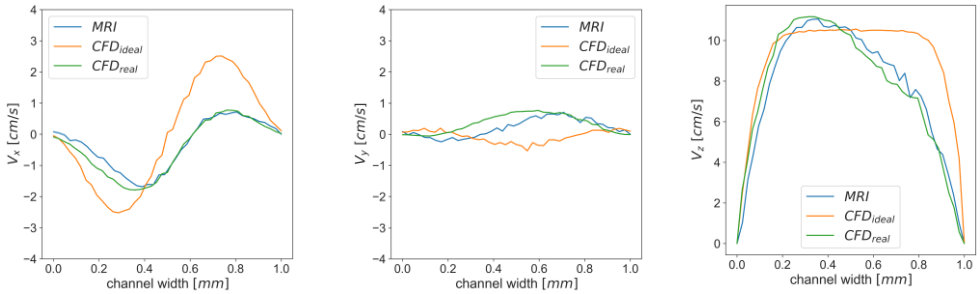

(c) slice position P2

CFD

ideal geometry

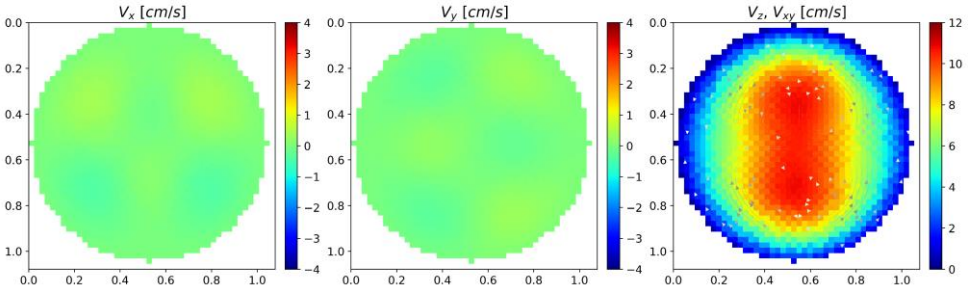

CFD

real geometry

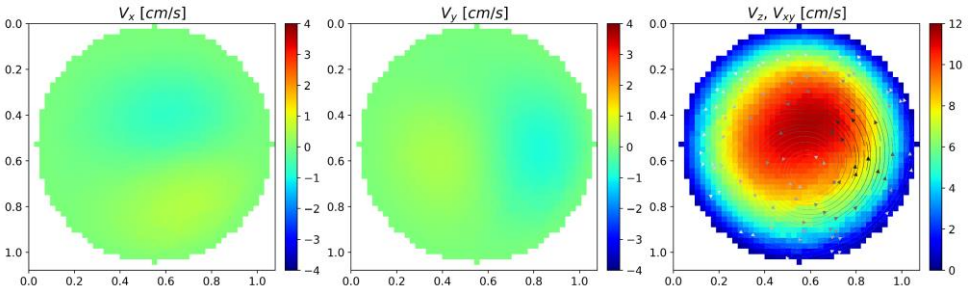

MRI

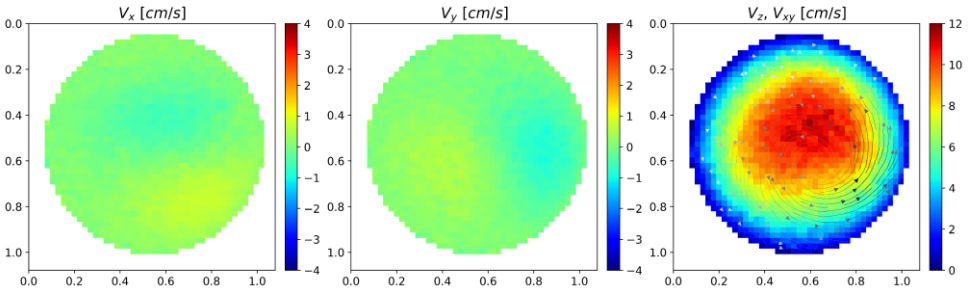

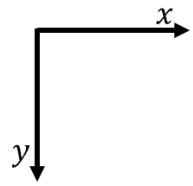

central profile

along x

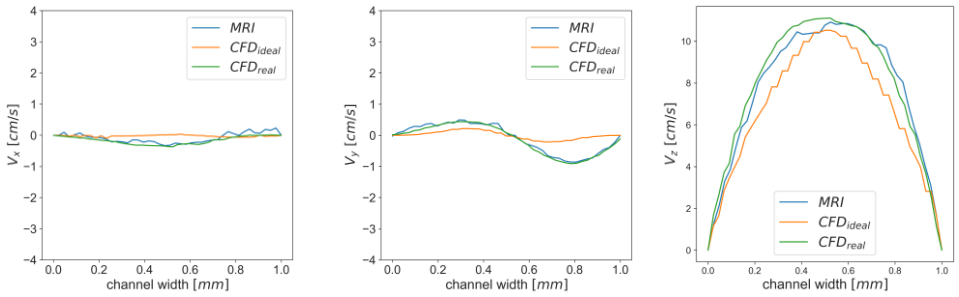

central profile

along y

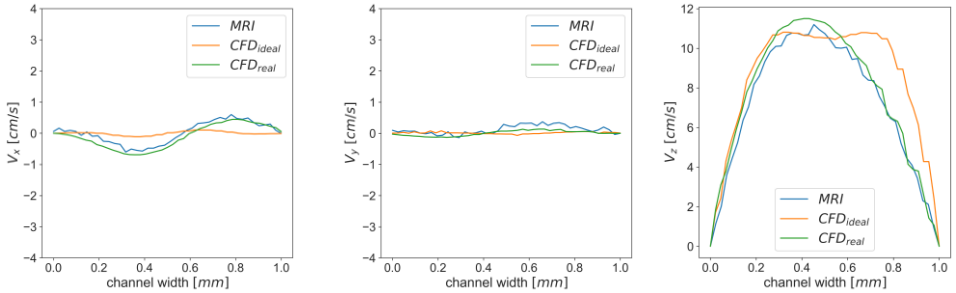

(d) slice position P3

CFD

ideal geometry

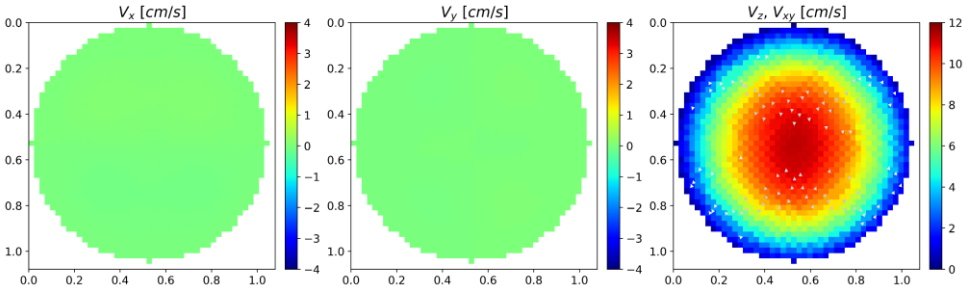

CFD

real geometry

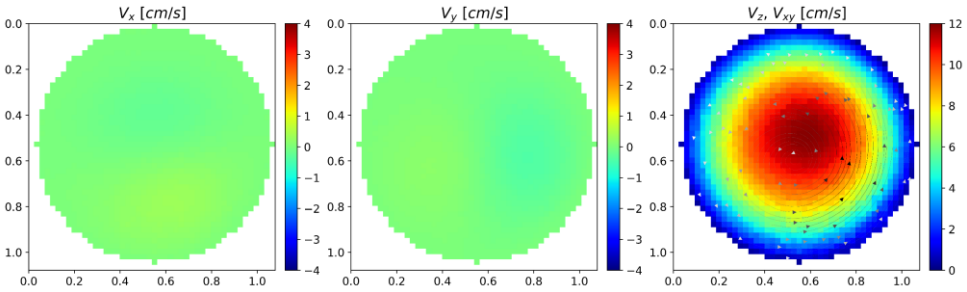

MRI

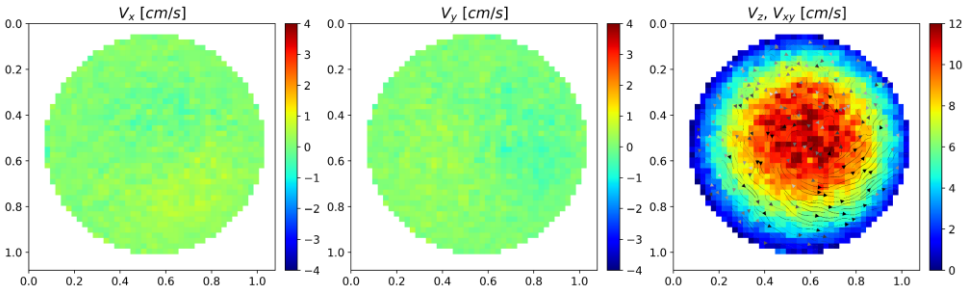

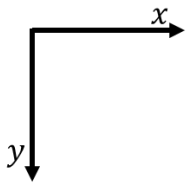

central profile along x

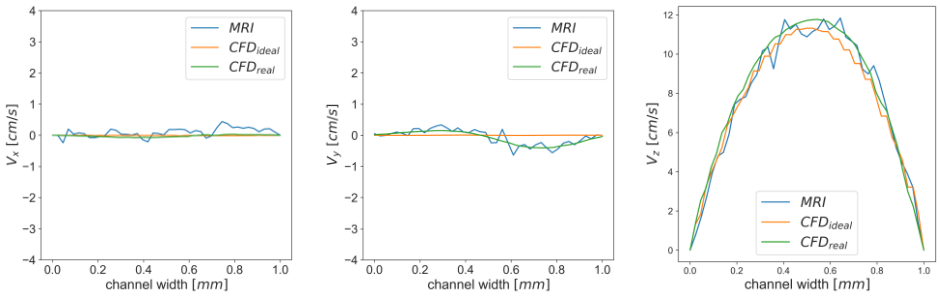

central profile along y

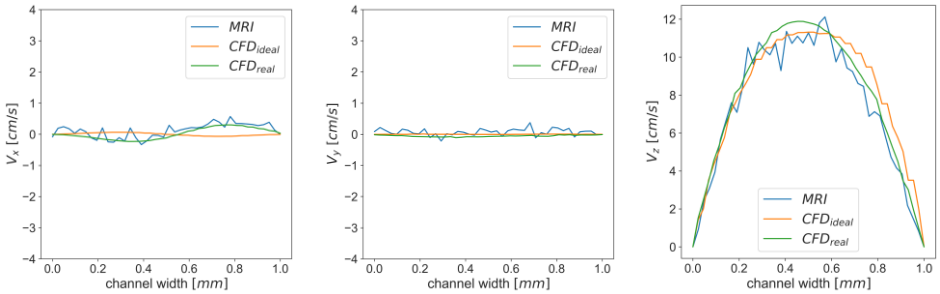

Figure 7: 2D Velocity maps obtained by CFD simulations on ideal and real geometry and by MRI measurements are presented from left to right respectively. The flow rate on each inlet is 1.4 ml/min corresponding to Re_{outlet} of 60. (a) 2D velocity maps measured in an orthogonal plane containing the three channels. From (b) to (d): 2D axial velocity maps at slice positions P1, P2 and P3 corresponding respectively to 2 mm, 3 mm and 4 mm from the mixing point. The transverse vector $\overrightarrow{V_{xy}}$ is represented with arrows superimposed to the velocity map of the $z-$component, the color of the arrows (black-and-white scale) and their width representing the norm of the vector. Velocity profiles along a centerline in the x and y directions allow quantitative comparison of MRI to CFD. The distances on the axes are in millimeters.

368

(a)

Slice position P1 Slice position P2

MRI

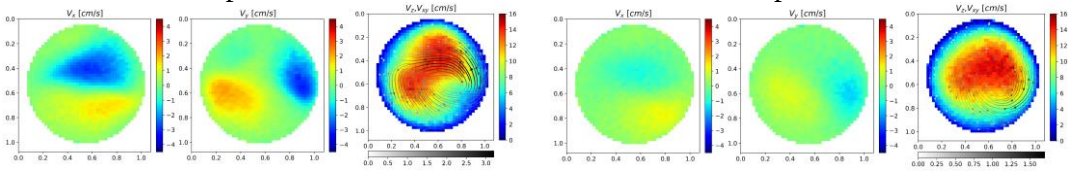

CFD real geometry

central profile along x

central profile along y

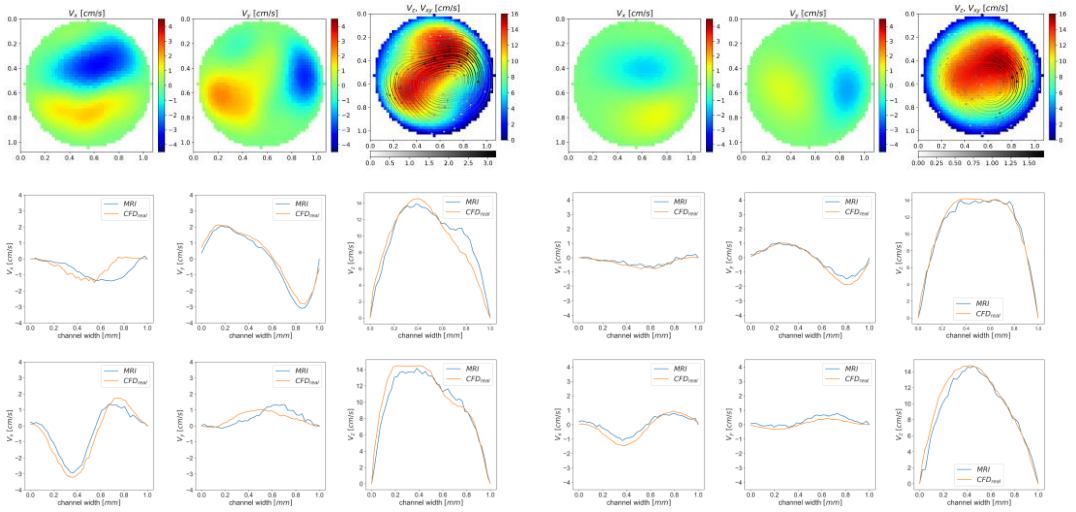

(b)

MRI

CFD real geometry

central profile along x

central profile along y

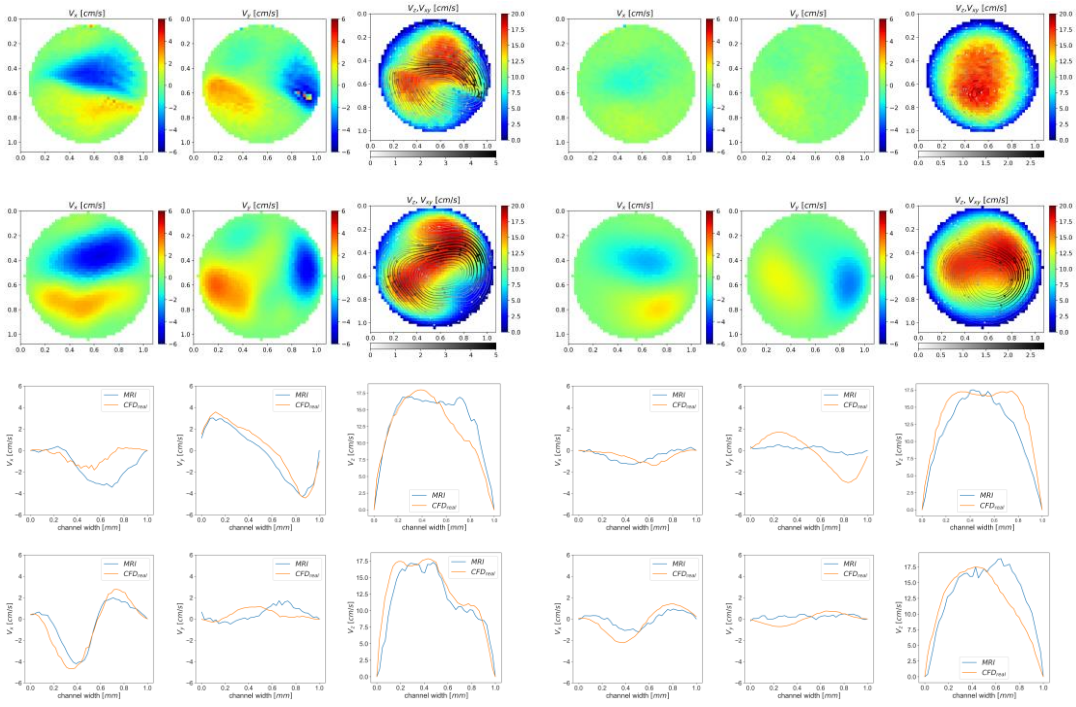

(c)

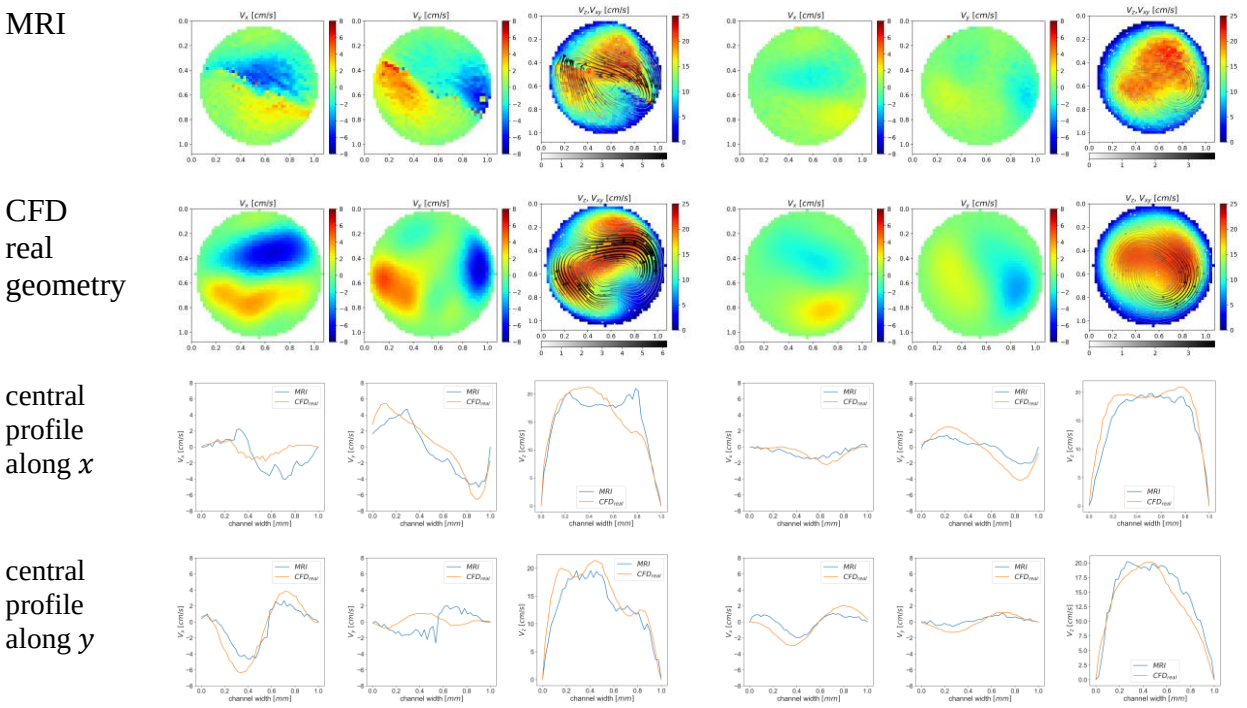

Figure 8: 3D velocity maps obtained by MRI measurements and by CFD simulations on real geometry for different Reynolds number on the outlet at slice positions P1 and P2 corresponding respectively to 2mm and 3mm from the mixing point. (a), (b) and (c) correspond to Re_{outlet} of 80, 102 and 123 respectively. Velocity profiles are plotted along central lines in the x and y directions for the quantitative comparison between CFD simulations (ideal and real geometries) and MRI measurements.

3.1.3. Effects of manufacturing defects on the mixing efficiency

In the previous sections, it has been shown that manufacturing defects have a great impact on the hydrodynamics downstream the mixing zone, and thus, they are expected to significantly influence the mixing efficiency. Mixing simulations (Section 2.3.3) were conducted in order to check this eventuality.

Simulations revealed that the exact micromixer geometry has a great impact on the mixing efficiency as can be seen from Figure 10. Indeed, in the case of the "ideal" geometry (and for all eight flow rates investigated), despite the presence of secondary flows, given the double symmetry

of the flow, the main contact zone between the two fluid streams remains quasi-planar which practically limits mixing to the sole effects of diffusion. In the case of the "real" geometry, the flow perturbation induced by the manufacturing defects engenders a larger contact zone between the two streams which is supposed to increase diffusive mixing (note that simulations probably overestimate the thickness of the mixing front because of numerical diffusion effects). Additionally, the large secondary flow cells engender engulfment of the two streams which is expected to enhance the mass-transfer efficiency. Hence, it is clear that these non-voluntary manufacturing defects have a positive impact on the mixing quality although they generate additional mechanical energy dissipation.

When increasing the flow rate, as inertial effects becomes larger, mixing efficiency is improved in both geometries. However, while this enhancement remains insufficient with the ideal design as the main contact zone remains quasi-planar, it is much more pronounced in the case of the real geometry as the contact zone becomes larger. Moreover, as mentioned in the previous section, for a flow rate of $4.2\ ml/min$, in the case of the real geometry, the presence of manufacturing chips induces some unsteadiness in the flow which is expected to further enhance the mixing quality.

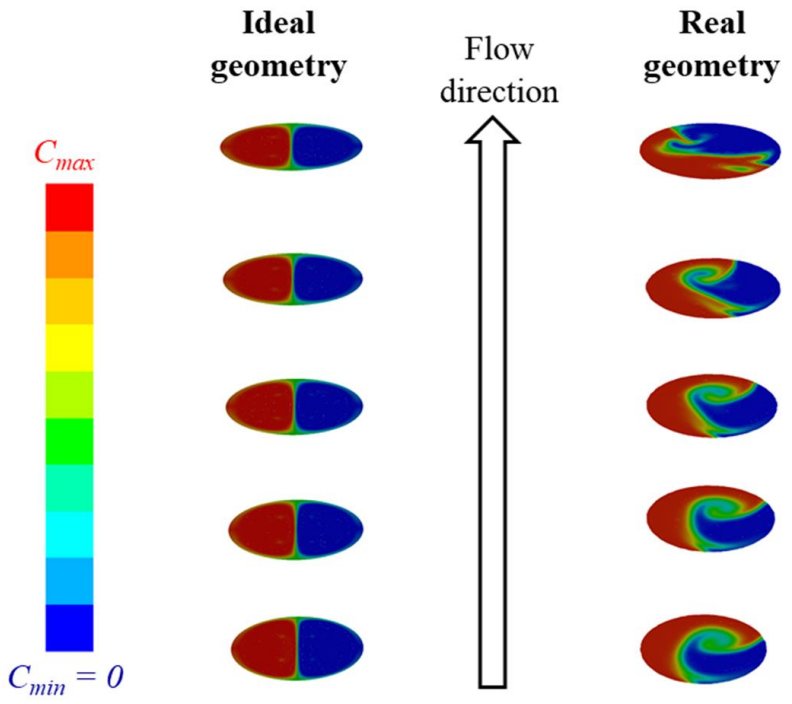

394

395 *Figure 9: Concentration field at sections located 3, 4, 5, 6 and 7 mm downstream of the mixing*
396 *point: case where the flow rate at each inlet is 3.4 ml/min.*

397

398 ## 4. Conclusion

399 In this study, NMR imaging methods were used to study the hydrodynamics occurring in the
400 mixing channel of a micromixer in an arrow configuration. A specific device was set up including
401 a home-made radiofrequency coil with reduced dimensions and adapted to the geometry and the
402 dimensions of the manufactured micromixer. In the homogeneity zone of the radiofrequency field
403 generated by the developed milli-coil, the signal-to-noise ratio was improved by a factor 7 in
404 comparison with a standard commercial hardware.

405 MRI measurements were performed for the imaging of the 3D velocity field in the micromixer.
406 On another hand, computational fluid dynamics (CFD) simulations of the hydrodynamics in the

device were carried out. The 2D velocity maps obtained by MRI measurements showed some different symmetries on the fluid flow evolution and on the development of the secondary flows compared to the CFD simulations performed on an "ideal" geometry of the micromixer. This comparison revealed that the flow field was sensitive to the presence of small manufacturing defects. Accounting for these imperfections in the numerical model (real geometry of the micromixer extracted by X-ray µCT) allowed obtaining, in the range of the flow rates investigated, a good agreement between experimental results and numerical data, hence confirming the potentiality of the developed NMR instrumentation for characterizing flow phenomena in millimetric devices.

As the flow field was very sensitive to the manufacturing defects, the mixing efficiency was also impacted. The simulations on the real geometry revealed that the defects engendered a larger contact zone between the two fluid streams and their engulfment. This is expected to enhance both mass-transfer and diffusive mixing.

References

Ahola, S., Casanova, F., Perlo, J., Münnemann, K., Blümich, B., & Stapf, S. (2006). Monitoring of fluid motion in a micromixer by dynamic NMRmicroscopy. *Lab Chip*, *6*(1), 90–95. https://doi.org/10.1039/B510708C

Ahola, S., Telkki, V.-V., & Stapf, S. (2012). Velocity distributions in a micromixer measured by NMR imaging. *Lab on a Chip*, *12*(10), 1823. https://doi.org/10.1039/c2lc21214e

Akpa, B. S., Matthews, S. M., Sederman, A. J., Yunus, K., Fisher, A. C., Johns, M. L., & Gladden, L. F. (2007). Study of Miscible and Immiscible Flows in a Microchannel Using Magnetic Resonance Imaging. *Analytical Chemistry*, *79*(16), 6128–6134. https://doi.org/10.1021/ac070364a

Bayareh, M., Ashani, M. N., & Usefian, A. (2020). Active and passive micromixers: A comprehensive review. *Chemical Engineering and Processing - Process Intensification*, *147*, 107771. https://doi.org/10.1016/j.cep.2019.107771

Blümich Bernhard. (2000). *NMR imaging of materials*. Clarendon Press Oxford University Press.

Bothe, D., Stemich, C., & Warnecke, H.-J. (2006). Fluid mixing in a T-shaped micro-mixer. *Chemical Engineering Science*, *61*(9), 2950–2958. https://doi.org/10.1016/j.ces.2005.10.060

Callaghan, P. T., & Xia, Y. (1991). Velocity and diffusion imaging in dynamic NMR microscopy. *Journal of Magnetic Resonance (1969)*, *91*(2), 326–352. https://doi.org/10.1016/0022-2364(91)90196-Z

Callaghan P. T. (1991). *Principles of nuclear magnetic resonance microscopy*. Clarendon press.

Caprihan, A., & Fukushima, E. (1990). Flow measurements by NMR. *Physics Reports*, *198*(4), 195–235. https://doi.org/10.1016/0370-1573(90)90046-5

Ciobanu, L., Jayawickrama, D. A., Zhang, X., Webb, A. G., & Sweedler, J. V. (2003). Measuring Reaction Kinetics by Using Multiple Microcoil NMR Spectroscopy. *Angewandte Chemie International Edition*, *42*(38), 4669–4672. https://doi.org/10.1002/anie.200351901

Commenge, J.-M., & Falk, L. (2011). Villermaux–Dushman protocol for experimental characterization of micromixers. *Chemical Engineering and Processing: Process Intensification*, *50*(10), 979–990. https://doi.org/10.1016/j.cep.2011.06.006

Chung, K. Y. (1993). Dean Vortices in Curved Tube Flow: 5. 3-D MRI and Numerical Analysis of the Velocity Field. *AIChE Journal*, 39(10), 1592-1602. https://doi.org/10.1002/aic.690391003

Dechow, J., Forchel, A., Lanz, T., & Haase, A. (2000). Fabrication of NMR — Microsensors for nanoliter sample volumes. *Microelectronic Engineering*, *53*(1–4), 517–519. https://doi.org/10.1016/S0167-9317(00)00368-3

Dreher, S., Kockmann, N., & Woias, P. (2009). Characterization of Laminar Transient Flow Regimes and Mixing in T-shaped Micromixers. *Heat Transfer Engineering*, *30*(1–2), 91–100. https://doi.org/10.1080/01457630802293480

Engler, M., Kockmann, N., Kiefer, T., & Woias, P. (2004). Numerical and experimental investigations on liquid mixing in static micromixers. *Chemical Engineering Journal*, *101*(1–3), 315–322. https://doi.org/10.1016/j.cej.2003.10.017

Eroglu, S., Gimi, B., Roman, B., Friedman, G., & Magin, R. L. (2003). NMR spiral surface microcoils: Design, fabrication, and imaging. *Concepts in Magnetic Resonance*, *17B*(1), 1–10. https://doi.org/10.1002/cmr.b.10068

Falk, L., & Commenge, J.-M. (2010). Performance comparison of micromixers. *Chemical Engineering Science*, *65*(1), 405–411. https://doi.org/10.1016/j.ces.2009.05.045

Ferrari, M., Moyne, C., & Stemmelen, D. (2018). Study of Dispersion in Porous Media by Pulsed Field Gradient NMR: Influence of the Fluid Rheology. *Transport in Porous Media*, *123*(1), 101–124. https://doi.org/10.1007/s11242-018-1027-0

Fu, R., Brey, W. W., Shetty, K., Gor'kov, P., Saha, S., Long, J. R., Grant, S. C., Chekmenev, E. Y., Hu, J., Gan, Z., Sharma, M., Zhang, F., Logan, T. M., Brüschweller, R., Edison, A., Blue, A., Dixon, I. R., Markiewicz, W. D., & Cross, T. A. (2005). Ultra-wide bore 900MHz high-resolution NMR at the National High Magnetic Field Laboratory. *Journal of Magnetic Resonance*, *177*(1), 1–8. https://doi.org/10.1016/j.jmr.2005.07.013

Galletti, C., Mariotti, A., Siconolfi, L., Mauri, R., & Brunazzi, E. (2019). Numerical investigation of flow regimes in T-shaped micromixers: Benchmark between finite volume and spectral

element methods. *The Canadian Journal of Chemical Engineering*, *97*(2), 528–541. https://doi.org/10.1002/cjce.23321

Gladden, L. F., & Alexander, P. (1996). Applications of nuclear magnetic resonance imaging in process engineering. *Measurement Science and Technology*, *7*(3), 423–435. https://doi.org/10.1088/0957-0233/7/3/026

Harel, E., & Pines, A. (2008). Spectrally resolved flow imaging of fluids inside a microfluidic chip with ultrahigh time resolution. *Journal of Magnetic Resonance*, *193*(2), 199–206. https://doi.org/10.1016/j.jmr.2008.04.037

Hessel, V., Löwe, H., & Schönfeld, F. (2005). Micromixers—A review on passive and active mixing principles. *Chemical Engineering Science*, *60*(8–9), 2479–2501. https://doi.org/10.1016/j.ces.2004.11.033

Hoult, D. I., & Richards, R. E. (2011). The signal-to-noise ratio of the nuclear magnetic resonance experiment. *Journal of Magnetic Resonance*, *213*(2), 329–343. https://doi.org/10.1016/j.jmr.2011.09.018

Hsieh, S.-S. (2013). Mixing efficiency of Y-type micromixers with different angles. *International Journal of Heat and Fluid Flow*, 10.

Ionin, B. I., & Ershov, B. A. (1995). *NMR Spectroscopy in Organic Chemistry*. Springer US. https://doi.org/10.1007/978-1-4684-1785-2

Klein, M., Perrin, J. C., Leclerc, S., Guendouz, L., Dillet, J. & Lottin, O. (2013). Spatially and Temporally Resolved Measurement of Water Distribution in Nafion Using NMR Imaging. *ECS Transactions*, 58 (1), 283-289. https://doi.org/10.1149/05801.0283ecst

497 Klein, M., Perrin, J.-C., Leclerc, S., Guendouz, L., Dillet, J., & Lottin, O. (2013). Anisotropy of
498 Water Self-Diffusion in a Nafion Membrane under Traction. *Macromolecules*, *46*(23),
499 9259–9269. https://doi.org/10.1021/ma401511t
500 Kovacs, H., Moskau, D., & Spraul, M. (2005). Cryogenically cooled probes—A leap in NMR
501 technology. *Progress in Nuclear Magnetic Resonance Spectroscopy*, *46*(2–3), 131–155.
502 https://doi.org/10.1016/j.pnmrs.2005.03.001
503 Lacey, M. E., Subramanian, R., Olson, D. L., Webb, A. G., & Sweedler, J. V. (1999). High-
504 Resolution NMR Spectroscopy of Sample Volumes from 1 nL to 10 μL. *Chemical Reviews*,
505 *99*(10), 3133–3152. https://doi.org/10.1021/cr980140f
506 Lee, C.-Y., & Fu, L.-M. (2018). Recent advances and applications of micromixers. *Sensors and*
507 *Actuators B: Chemical*, *259*, 677–702. https://doi.org/10.1016/j.snb.2017.12.034
508 Lobasov, A. S., Minakov, A. V., Kuznetsov, V. V., Rudyak, V. Ya., & Shebeleva, A. A. (2018).
509 Investigation of mixing efficiency and pressure drop in T-shaped micromixers. *Chemical*
510 *Engineering and Processing - Process Intensification*, *134*, 105–114.
511 https://doi.org/10.1016/j.cep.2018.10.012
512 Massin, C., Boero, G., Vincent, F., Abenhaim, J., Besse, P.-A., & Popovic, R. S. (2002). High-Q
513 factor RF planar microcoils for micro-scale NMR spectroscopy. *Sensors and Actuators A:*
514 *Physical*, *97–98*, 280–288. https://doi.org/10.1016/S0924-4247(01)00847-0
515 Meier, R. C., Höfflin, J., Badilita, V., Wallrabe, U., & Korvink, J. G. (2014). Microfluidic
516 integration of wirebonded microcoils for on-chip applications in nuclear magnetic
517 resonance. *Journal of Micromechanics and Microengineering*, *24*(4), 045021.
518 https://doi.org/10.1088/0960-1317/24/4/045021
519 Mendez, D. L. M., Lemaitre, C., Castel C., Ferrari, M., Simonaire, H. & Favre E. (2017).
520 Membrane contactors for process intensification of gas absorption into physical solvents:

Impact of dean vortices. Journal of Membrane Science, 530, 20-32, http://dx.doi.org/10.1016/j.memsci.2017.02.016

Milc, K. W., Serial, M. R., Philippi, J., Dijksman, J. A., van Duynhoven, J. P. M., & Terenzi, C. (2022). Validation of temperature-controlled rheo-MRI measurements in a submillimeter-gap Couette geometry. *Magnetic Resonance in Chemistry*, *60*(7), 606–614. https://doi.org/10.1002/mrc.5157

Murphree, D., Cahn, S. B., Rahmlow, D., & DeMille, D. (2007). An easily constructed, tuning free, ultra-broadband probe for NMR. *Journal of Magnetic Resonance*, *188*(1), 160–167. https://doi.org/10.1016/j.jmr.2007.05.025

Oliveira, A. V. S., Stemmelen, D., Leclerc, S., Glantz, T., Labergue, A., Repetto, G., & Gradeck, M. (2020). Velocity field and flow redistribution in a ballooned 7×7 fuel bundle measured by magnetic resonance velocimetry. *Nuclear Engineering and Design*, *369*, 110828. https://doi.org/10.1016/j.nucengdes.2020.110828

Olson, D. L., Peck, T. L., Webb, A. G., Magin, R. L., & Sweedler, J. V. (1995). High-Resolution Microcoil ^{1}H-NMR for Mass-Limited, Nanoliter-Volume Samples. *Science*, *270*(5244), 1967–1970. https://doi.org/10.1126/science.270.5244.1967

Peck, T. L., Magin, R. L., & Lauterbur, P. C. (1995). Design and Analysis of Microcoils for NMR Microscopy. *Journal of Magnetic Resonance, Series B*, *108*(2), 114–124. https://doi.org/10.1006/jmrb.1995.1112

Peng, K., Xu, F., Yang, L., Yao, C., & Chen, G. (2022). Dean instability and vortex-induced mixing for two miscible fluids in T-micromixers. *Chemical Engineering and Processing - Process Intensification*, *176*, 108975. https://doi.org/10.1016/j.cep.2022.108975

Perrin, J.-C., Waldner, C., Bossu, J., Chatterjee, A. & Hirn, U. (2022). Real time monitoring of the through thickness moisture profile of thin sheets using NMR. *Chemical Engineering Science*, 251, 117464. https://doi.org/10.1016/j.ces.2022.117464

Pettegrew, J. W. (2012). *NMR: Principles and Applications to Biomedical Research*. Springer Science & Business Media.

Robert M., Kaddouri A. E., Perrin J.-C., Leclerc S. & Lottin O. (2018). Towards a NMR-Based Method for Characterizing the Degradation of Nafion XL Membranes for PEMFC. *Journal of The Electrochemical Society*, 165, n°6F3209-F3216. https://doi.org/10.1149/2.0231806jes

Seymour, J. D., & Callaghan, P. T. (1997). Generalized approach to NMR analysis of flow and dispersion in porous media. *AIChE Journal*, *43*(8), 2096–2111. https://doi.org/10.1002/aic.690430817

Stapf, S., & Han, S.-I. (2006). *NMR Imaging in Chemical Engineering*. John Wiley & Sons, Incorporated. http://ebookcentral.proquest.com/lib/ulorraine/detail.action?docID=481636

Trumbull, J. D., Glasgow, I. K., Beebe, D. J., & Magin, R. L. (2000). Integrating microfabricated fluidic systems and NMR spectroscopy. *IEEE Transactions on Biomedical Engineering*, *47*(1), 3–7. https://doi.org/10.1109/10.817611

Webb, A. G. (2008). Microcoil nuclear magnetic resonance spectroscopy. In *NMR Spectroscopy in Pharmaceutical Analysis* (p. 48).

Webb, A. G. (2012). Increasing the Sensitivity of Magnetic Resonance Spectroscopy and Imaging. *Analytical Chemistry*, *84*(1), 9–16. https://doi.org/10.1021/ac201500v

Webb, A. G. (2013). Radiofrequency microcoils for magnetic resonance imaging and spectroscopy. *Journal of Magnetic Resonance*, *229*, 55–66. https://doi.org/10.1016/j.jmr.2012.10.004

Wensink, H., Benito-Lopez, F., Hermes, D. C., Verboom, W., Gardeniers, H. J. G. E., Reinhoudt, D. N., & van den Berg, A. (2005). Measuring reaction kinetics in a lab-on-a-chip by microcoil NMR. *Lab on a Chip*, *5*(3), 280. https://doi.org/10.1039/b414832k

Woytasik, M., Grandchamp, J.-P., Dufour-Gergam, E., Gilles, J.-P., Megherbi, S., Martincic, E., Mathias, H., & Crozat, P. (2006). Two- and three-dimensional microcoil fabrication process for three-axis magnetic sensors on flexible substrates. *Sensors and Actuators A: Physical*, *132*(1), 2–7. https://doi.org/10.1016/j.sna.2006.06.062

Wüthrich, K. (1990). Protein structure determination in solution by NMR spectroscopy. *Journal of Biological Chemistry*, *265*(36), 22059–22062. https://doi.org/10.1016/S0021-9258(18)45665-7

Zhang, J., & Balcom, B. J. (2010). Parallel-plate RF resonator imaging of chemical shift resolved capillary flow. *Magnetic Resonance Imaging*, *28*(6), 826–833. https://doi.org/10.1016/j.mri.2010.03.033

Zhang, X., & Webb, A. G. (2005). Magnetic Resonance Microimaging and Numerical Simulations of Velocity Fields Inside Enlarged Flow Cells Used for Coupled NMR Microseparations. *Analytical Chemistry*, *77*(5), 1338–1344. https://doi.org/10.1021/ac048532b

Acknowledgements

The authors would like to thank Fadi Sharif (GREEN laboratory, Université de Lorraine) for his help during the fabrication of the NMR microcoil, and specifically during the etching on Kapton substrate.

Funding

588 This study was partially funded by the “pôle EMPP” and Fédération de recherche Jacques
589 Villermaux, Université de Lorraine, “Micro-MIX” project.

3D Magnetic resonance velocimetry for hydrodynamics characterization in microdevices: application to micromixers and comparison to CFD simulations

Feryal Guerroudj[1], Laouès Guendouz[1], Rainier Hreiz[2], Jean-Marc Commenge[2], Jérémy Bianchin[1], Christophe Morlot[3], Tien Dung Le[1] and Jean-Christophe Perrin[1*]

[*] to whom correspondence should be addressed: jean-christophe.perrin@univ-lorraine.fr

[1] Université de Lorraine, CNRS, LEMTA, F-54000 Nancy, France
[2] Université de Lorraine, CNRS, LRGP, F-54000 Nancy, France
[3] Univ Lorraine, CNRS, GeoRessources Lab, Blvd Aiguillettes, BP 70239, F-54506 Vandoeuvre Les Nancy, France

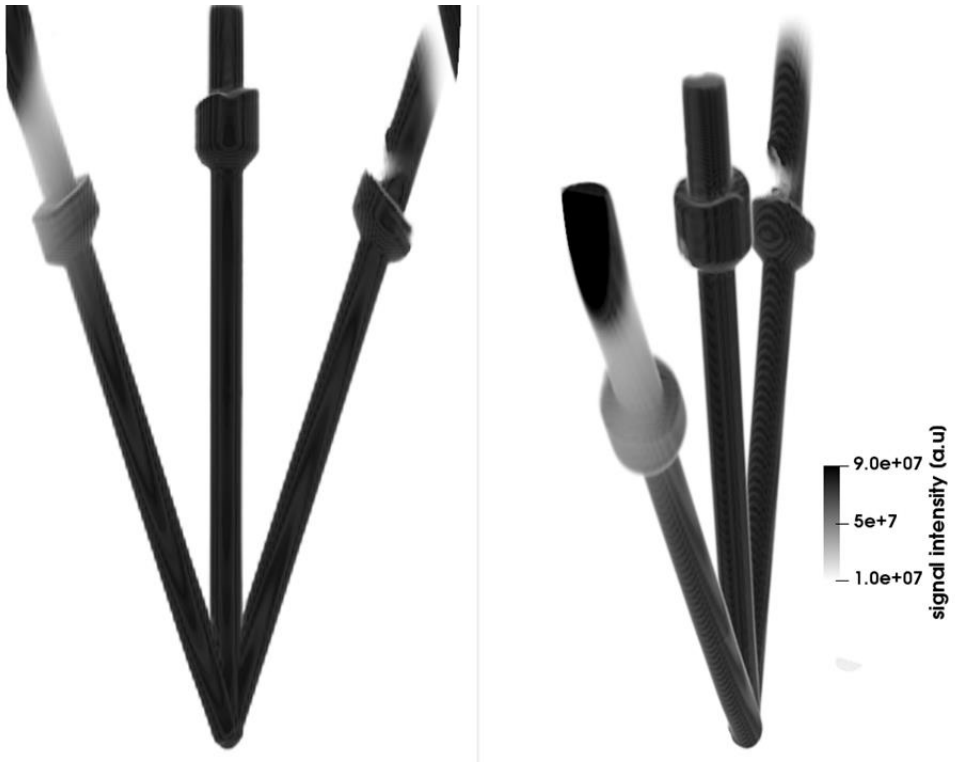

(a) (b)

Fig.S1: visualization of the 3D NMR signal intensity image on the Paraview software. Front view (a) and side view (b) of the machined micromixer filled with the copper sulfate solution

(a)

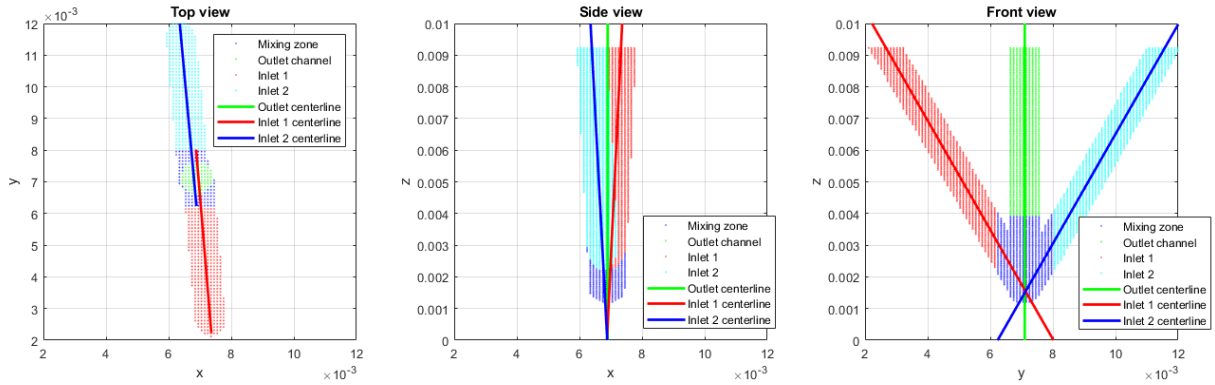

(b)

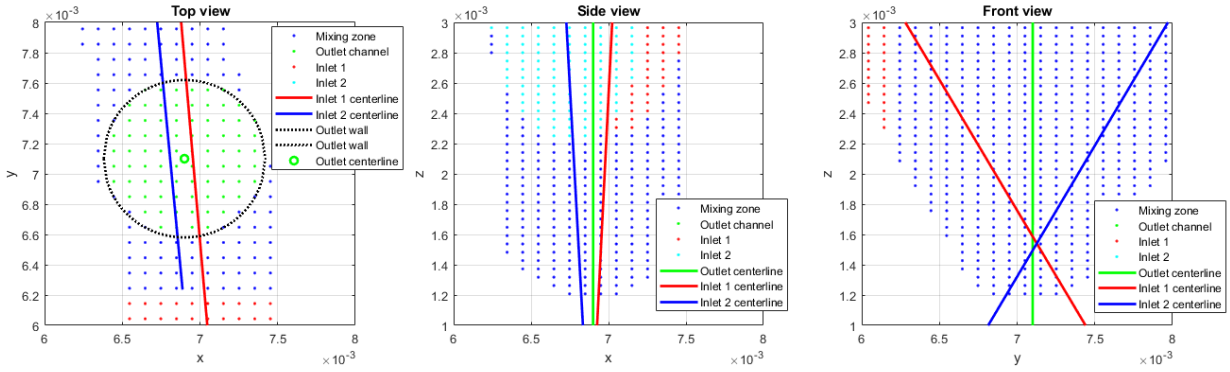

Fig.S2 : analysis and quantification of the misalignment of the three axes of the micromixer channels. (a) Views in 3 cross-sectional planes of the projections of the points in each channel and of the centerlines which constitute the axes of the microchannels. (b) Zooms on the three views near the mixing point, showing misalignment of the three microchannels: the two inlet centerlines and the outlet centerline did not meet exactly at the mixing point. The measured distances between the axes were about 90 µ*m and* 55 µ*m*

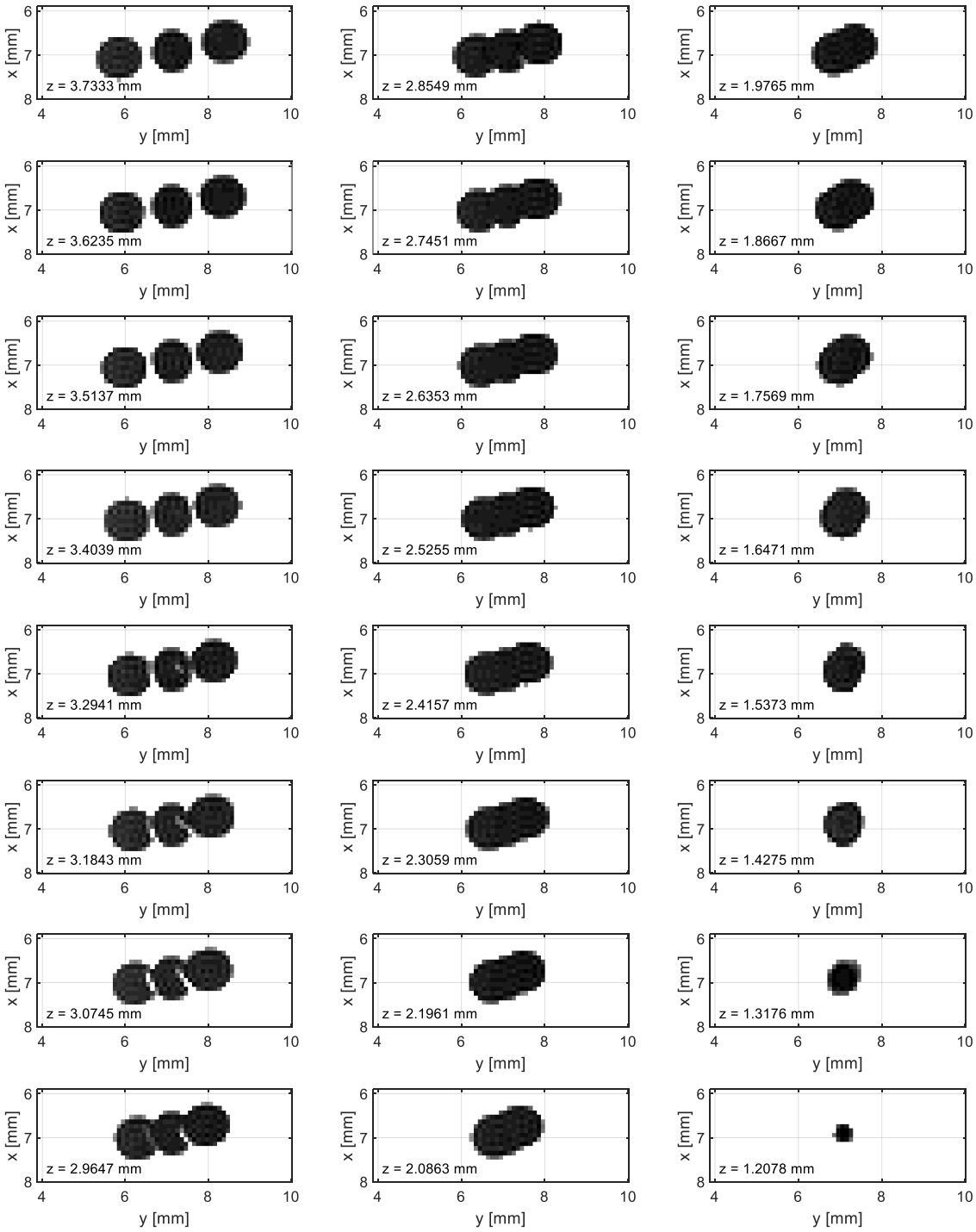

Fig.S3: Analysis of the images near the intersection of the 3 microchannels. Views of the sections of the 3 channels at different heights from the bottom of the micromixer, showing the presence of PMMA residues.

(a) (b)

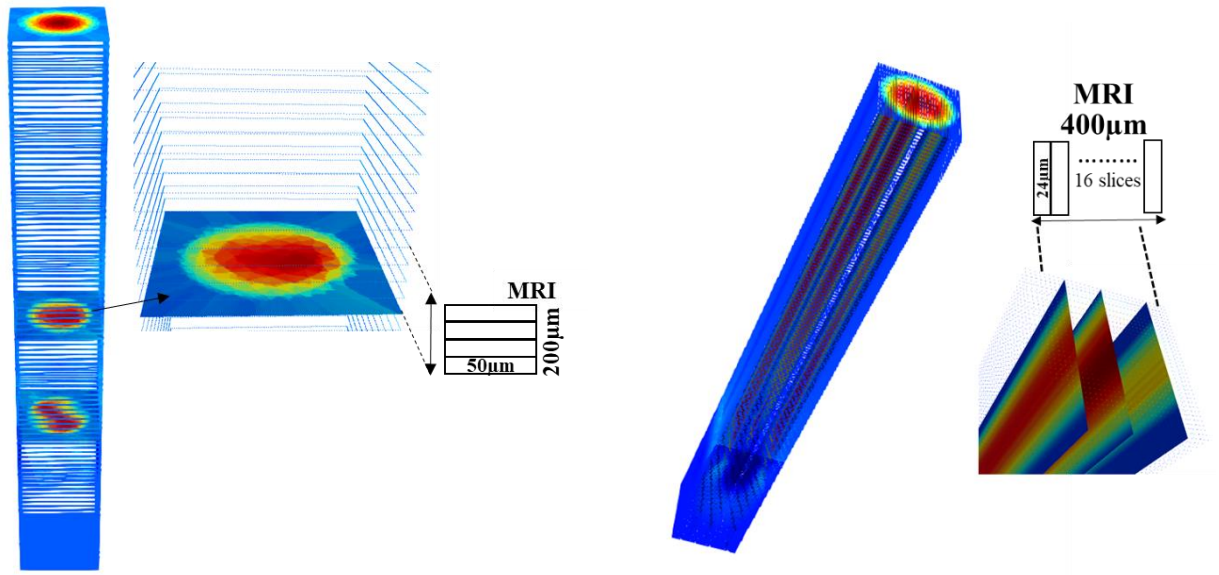

Fig.S4: interpolation of CFD data over coarser grid to correspond to MRI measurement conditions. (a) for axial images and (b) for images in planes orthogonal to the axial images. Construction of a uniform mesh with the "PointVolume Interpolator" function of Paraview. Reconstruction of the resampled data with Python as 3D matrices for each velocity component to perform averaging and display the results.

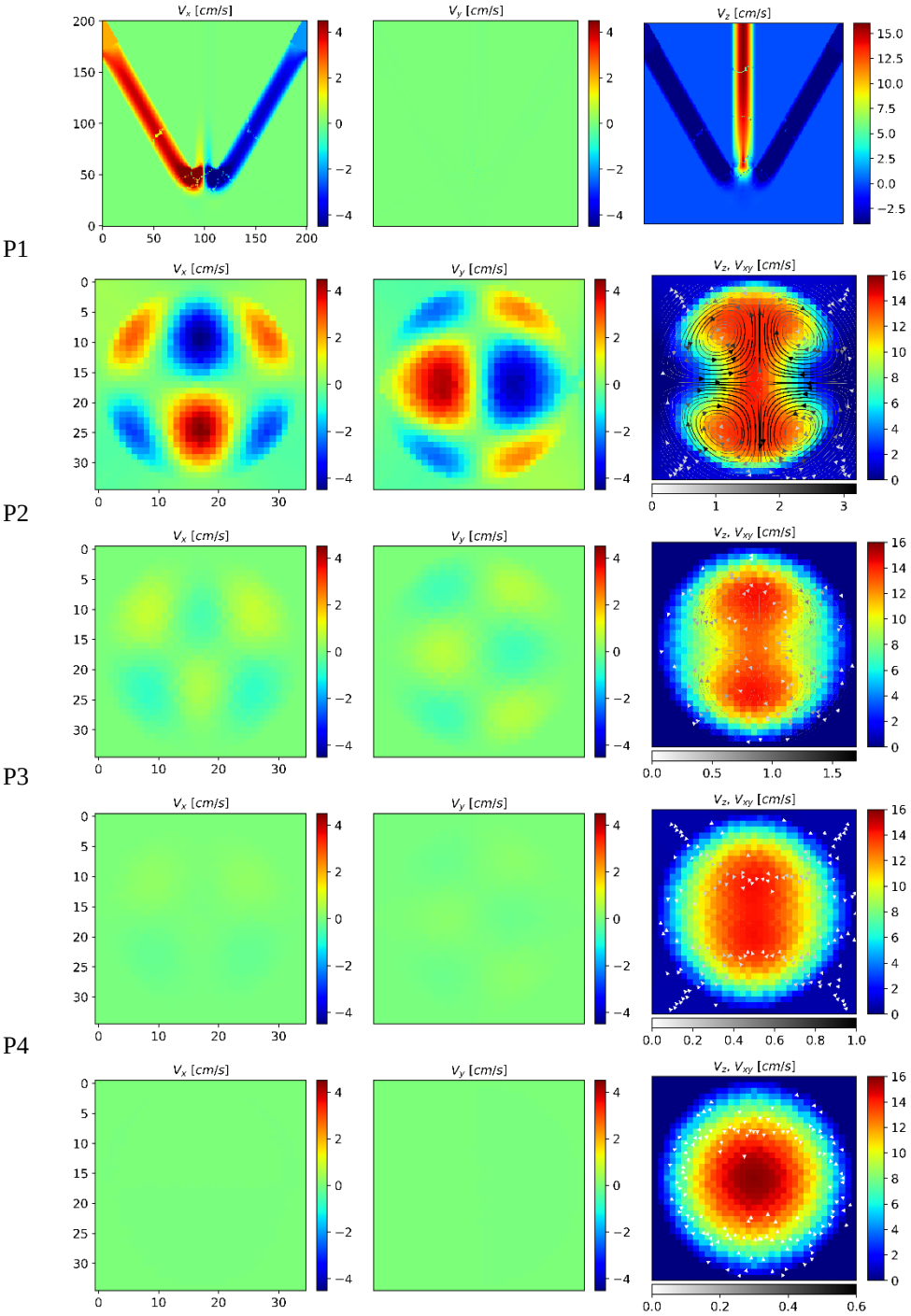

Fig.S5: 3D v*elocity maps obtained with CFD simulation on ideal geometry of the micromixer. The flow rate on each inlet is 1.9ml/min corresponding to* Re_{outlet} *of 80. The velocity maps in the orthogonal plane to the main flow direction are obtained at slice positions P1, P2, P3 and P4 corresponding respectively to 2mm, 3mm, 4mm and 7mm from the mixing point.*

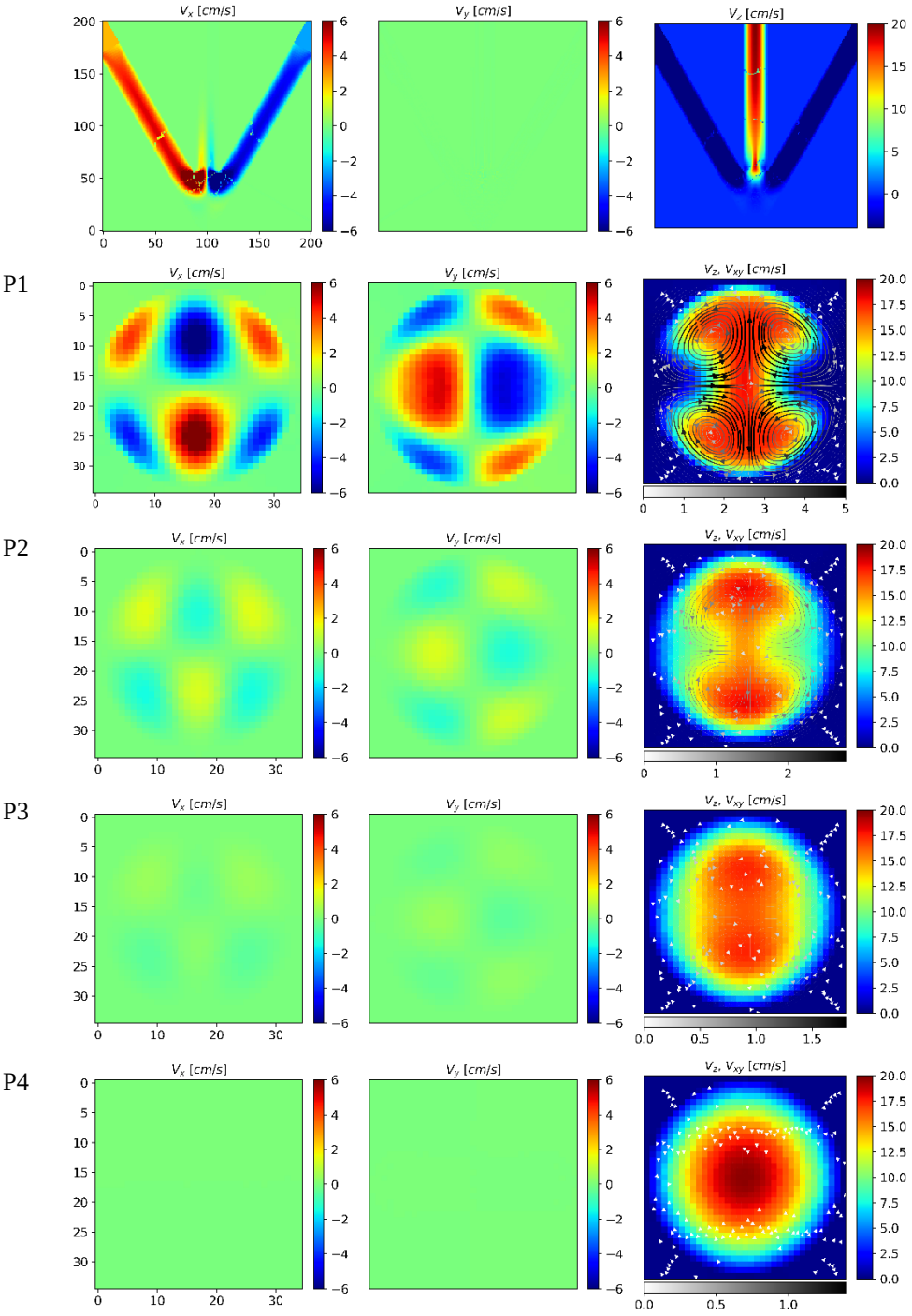

Fig.S6: 3D v*elocity maps obtained with CFD simulation on ideal geometry of the micromixer. The flow rate on each inlet is 2.4ml/min corresponding to* Re_{outlet} *of 102. The velocity maps in the orthogonal plane to the main flow direction are obtained at slice positions P1, P2, P3 and P4 corresponding respectively to 2mm, 3mm, 4mm and 7mm from the mixing point.*

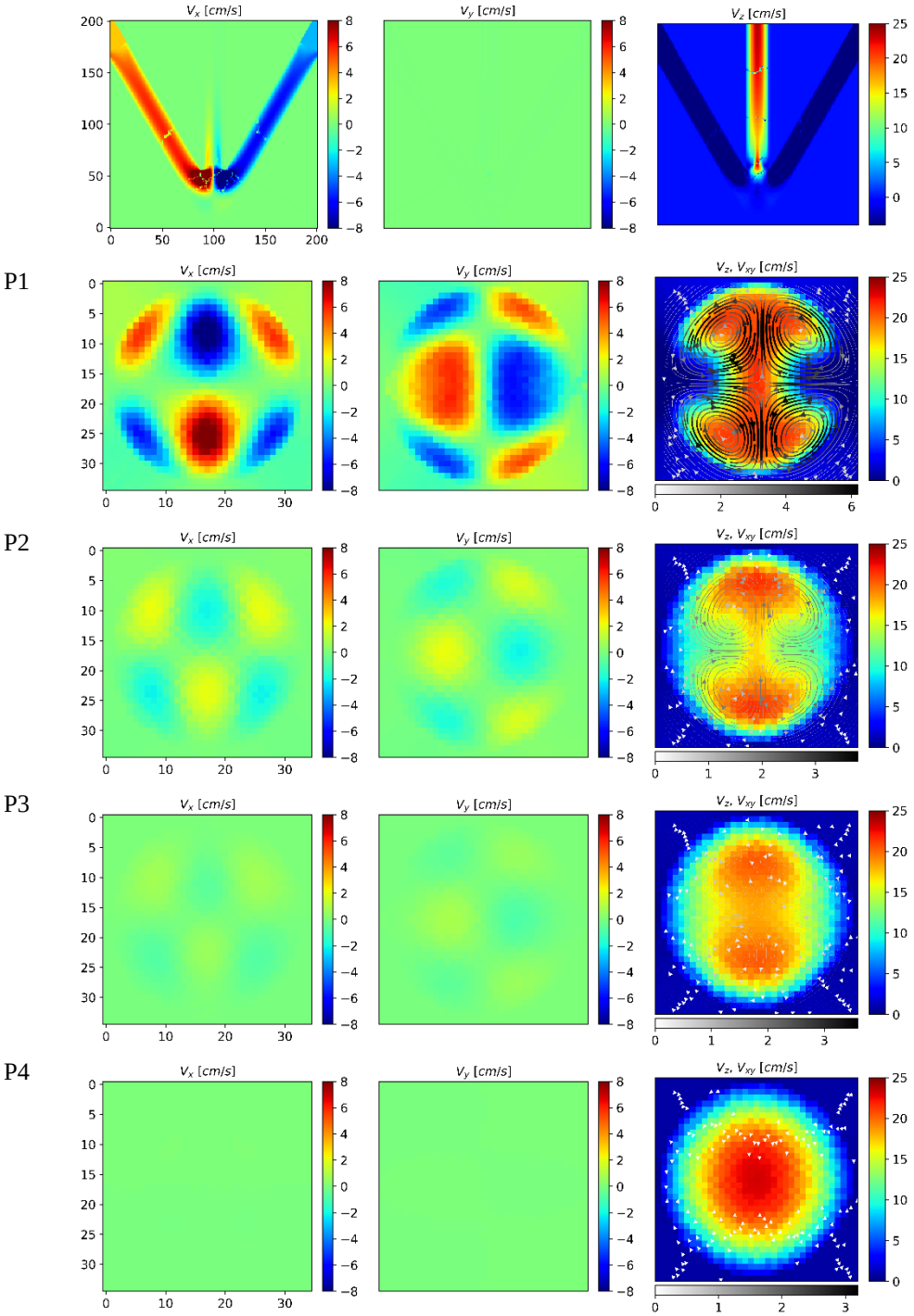

Fig.S7: 3D v*elocity maps obtained with CFD simulation on ideal geometry of the micromixer. The flow rate on each inlet is 2.9ml/min corresponding to* Re_{outlet} *of 123. The velocity maps in the orthogonal plane to the main flow direction are obtained at slice positions P1, P2, P3 and P4 corresponding respectively to 2mm, 3mm, 4mm and 7mm from the mixing point.*

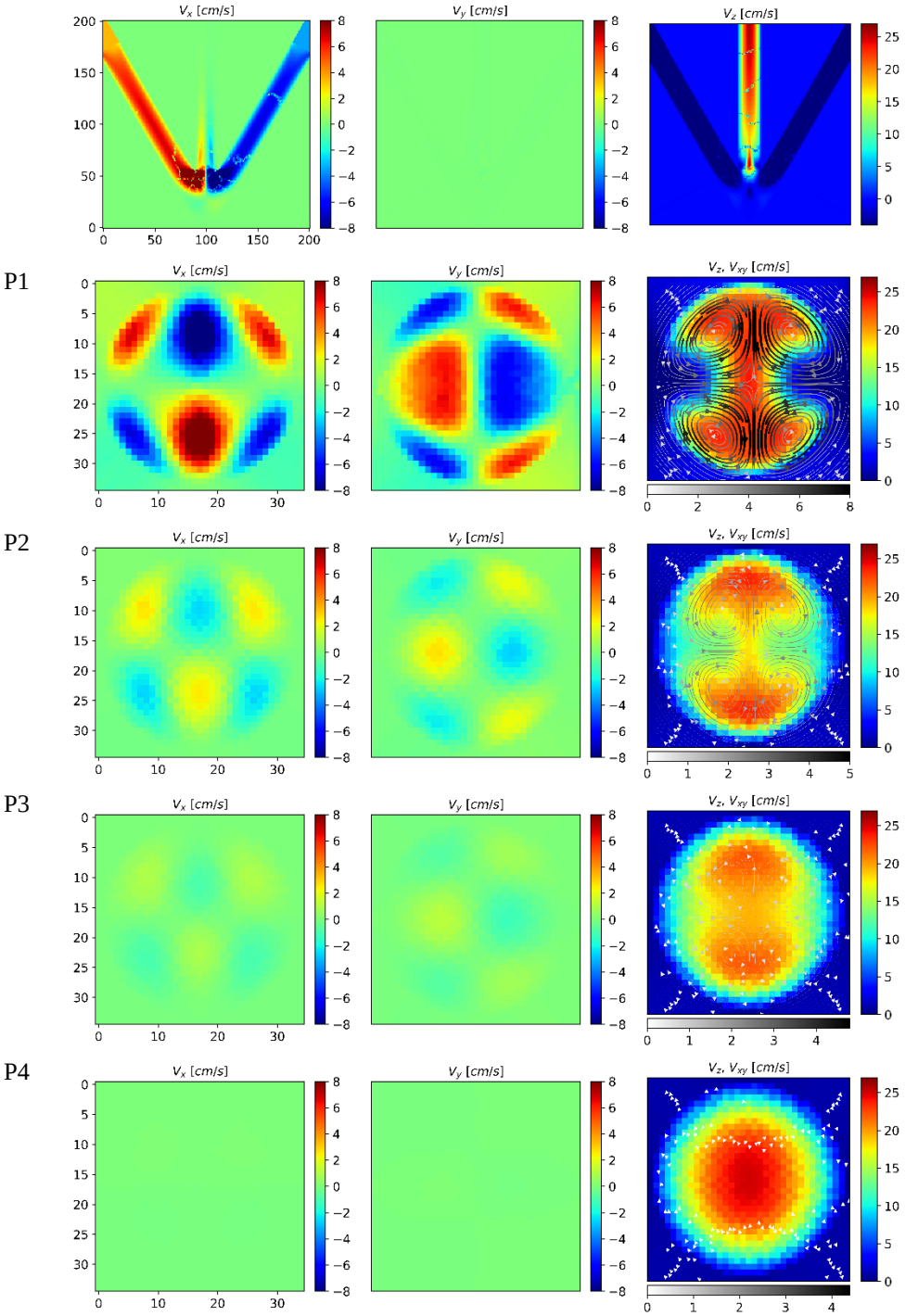

Fig.S8: 3D v*elocity maps obtained with CFD simulation on ideal geometry of the micromixer. The flow rate on each inlet is 3.2ml/min corresponding to* Re_{outlet} *of 136. The velocity maps in the orthogonal plane to the main flow direction are obtained at slice positions P1, P2, P3 and P4 corresponding respectively to 2mm, 3mm, 4mm and 7mm from the mixing point.*

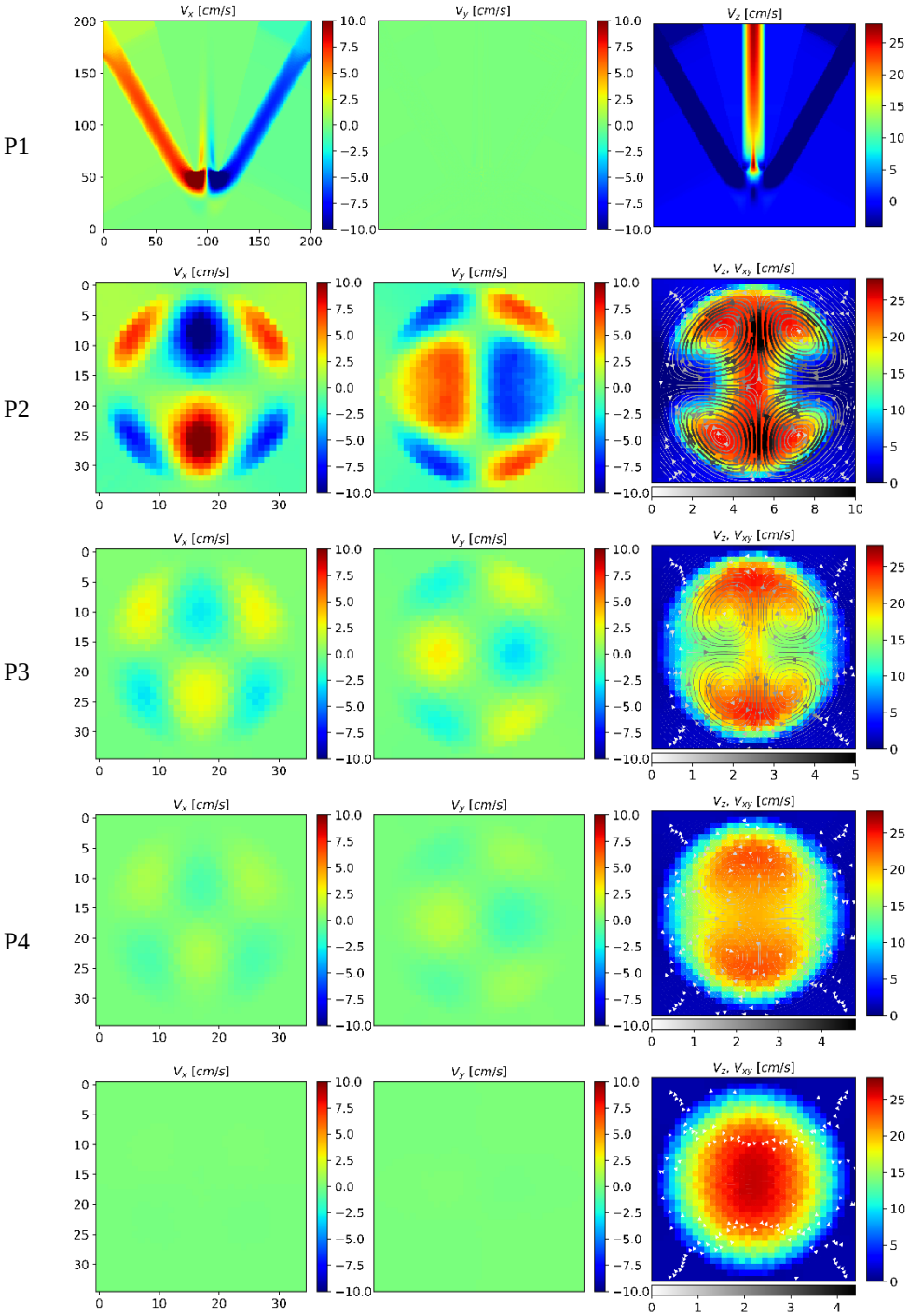

Fig.S9: 3D v*elocity maps obtained with CFD simulation on ideal geometry of the micromixer. The flow rate on each inlet is 3.4ml/min corresponding to* Re_{outlet} *of 144. The velocity maps in the orthogonal plane to the main flow direction are obtained at slice positions P1, P2, P3 and P4 corresponding respectively to 2mm, 3mm, 4mm and 7mm from the mixing point.*

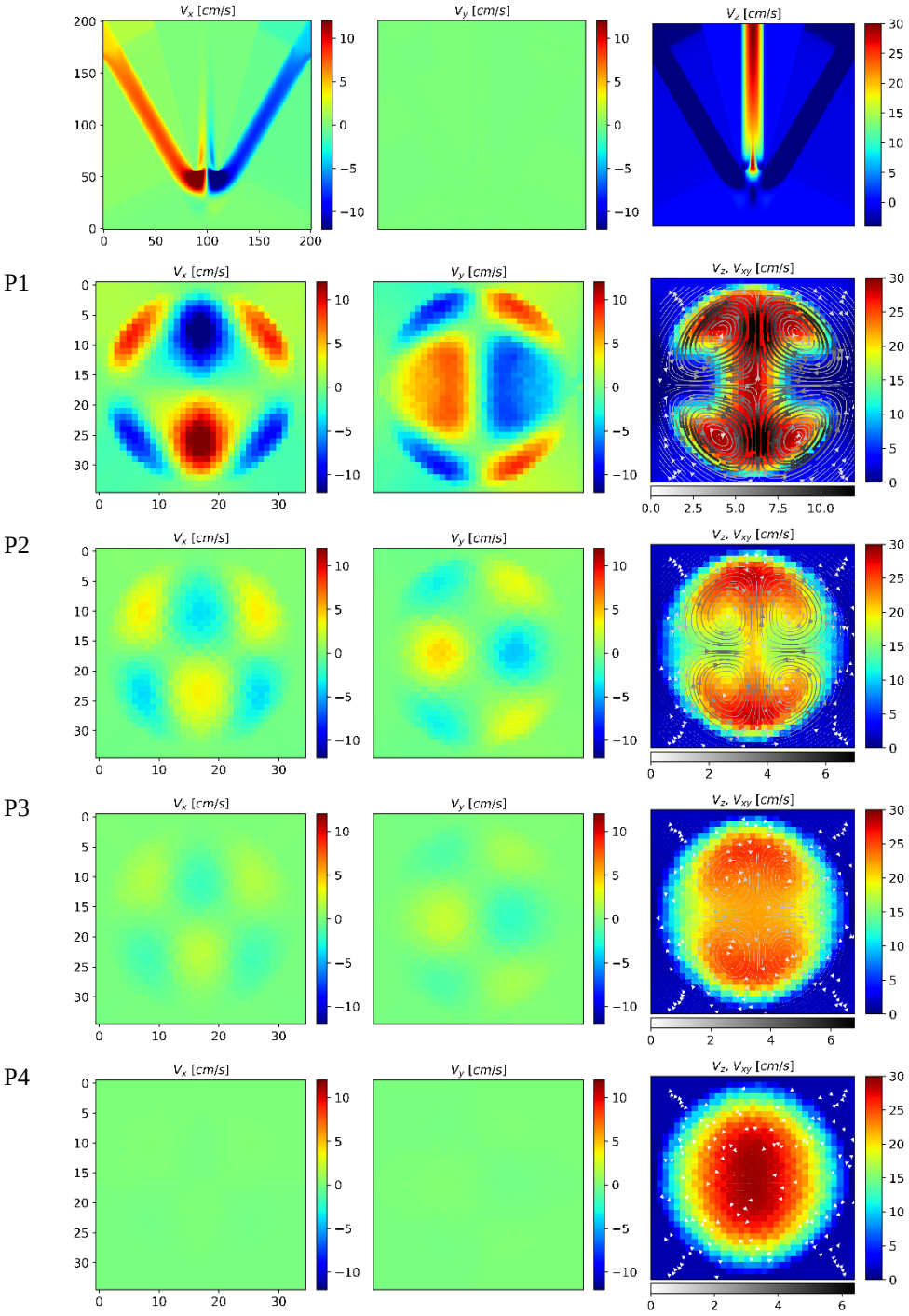

Fig.S10: 3D v*elocity maps obtained with CFD simulation on ideal geometry of the micromixer. The flow rate on each inlet is 3.9ml/min corresponding to* Re_{outlet} *of 165. The velocity maps in the orthogonal plane to the main flow direction are obtained at slice positions P1, P2, P3 and P4 corresponding respectively to 2mm, 3mm, 4mm and 7mm from the mixing point.*

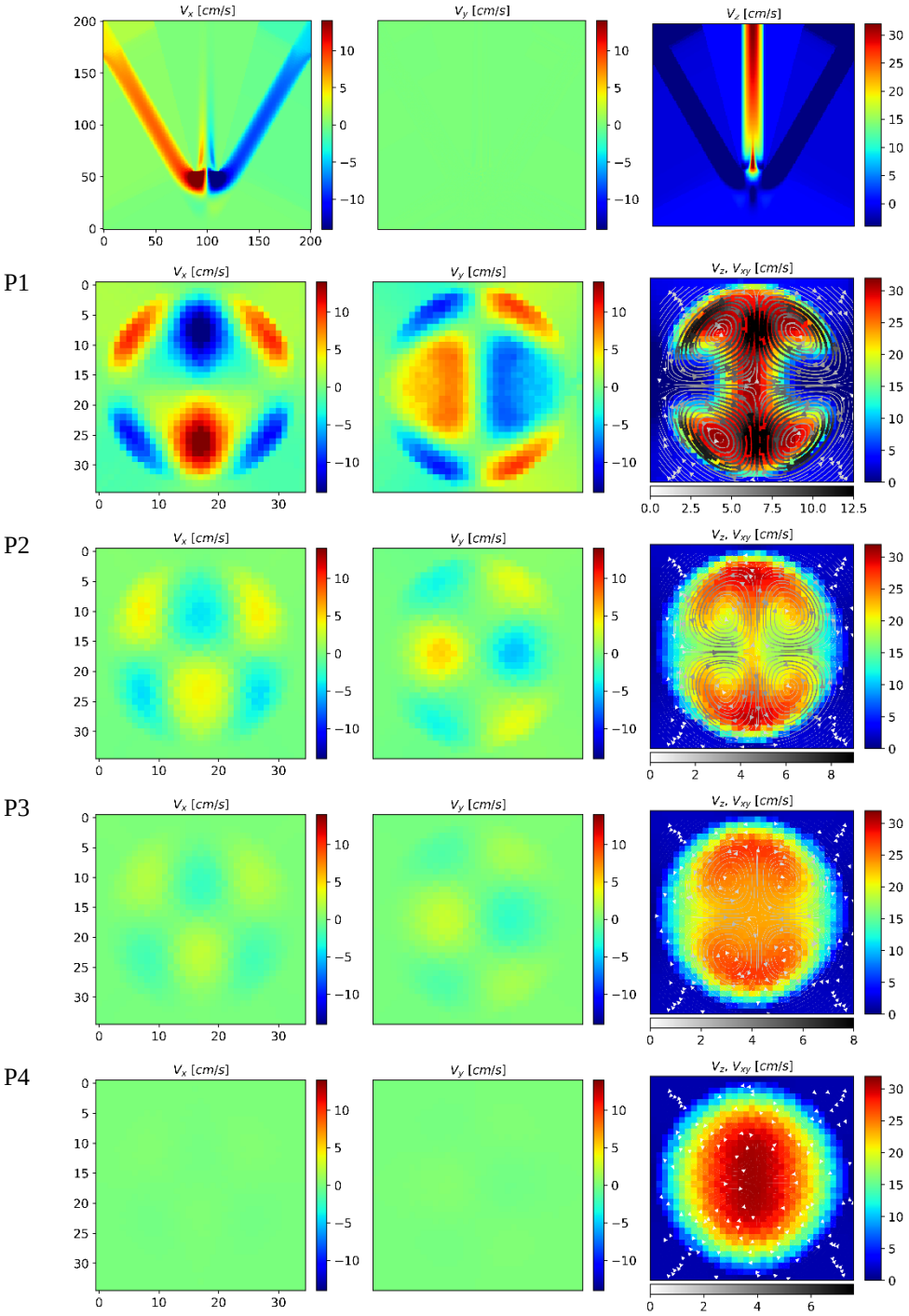

Fig.S11: 3D v*elocity maps obtained with CFD simulation on ideal geometry of the micromixer. The flow rate on each inlet is 4.2ml/min corresponding to* Re_{outlet} *of 178. The velocity maps in the orthogonal plane to the main flow direction are obtained at slice positions P1, P2, P3 and P4 corresponding respectively to 2mm, 3mm, 4mm and 7mm from the mixing point.*

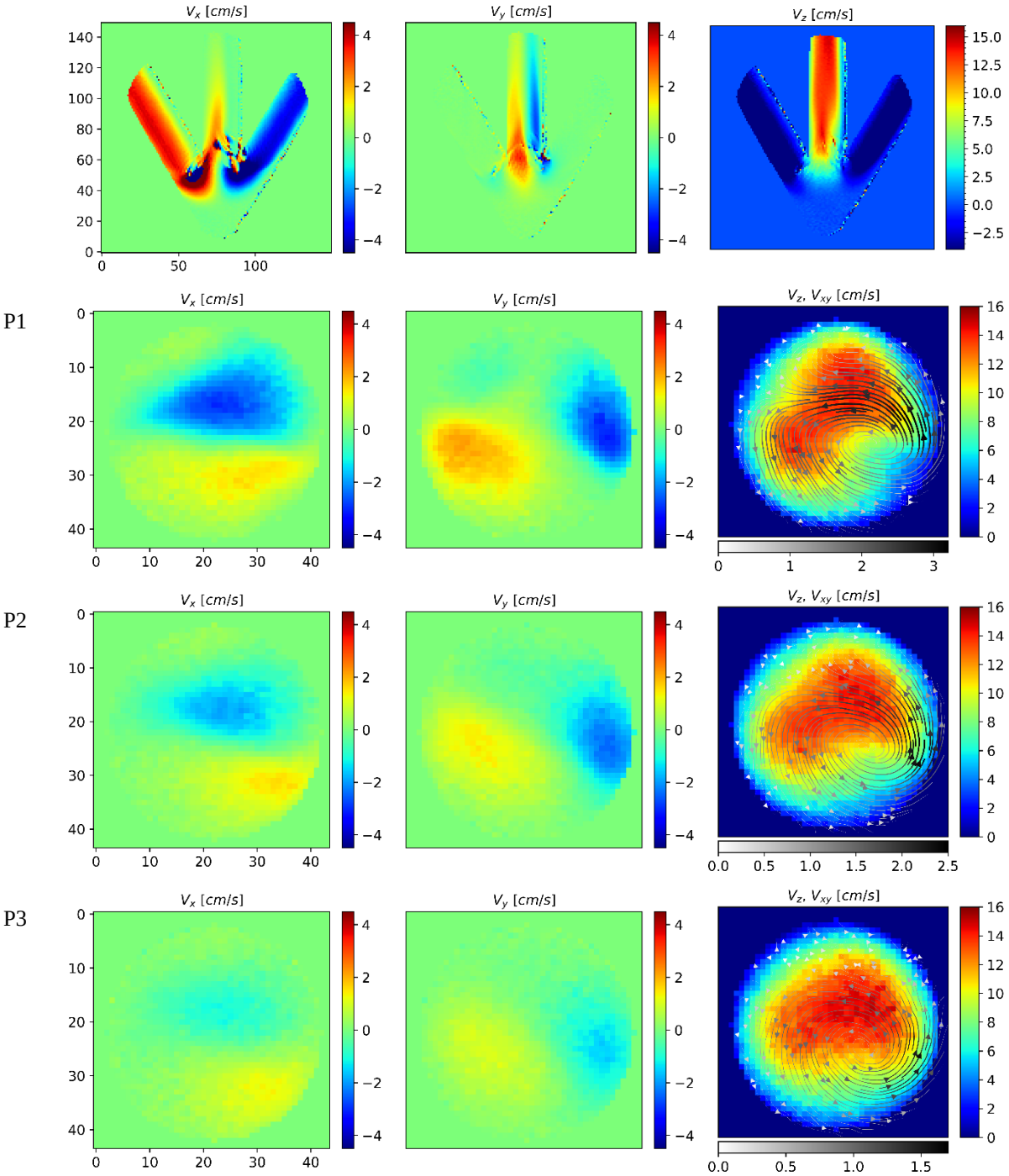

Fig.S12: 3D *velocity maps obtained with the developed milli-coil. The flow rate on each inlet is 1.9ml/min corresponding to* Re_{outlet} *of 80. The velocity maps in the orthogonal plane to the main flow direction are obtained at slice positions P1, P2 and P3 corresponding respectively to 2mm, 2.5mm and 3mm from the mixing point.*

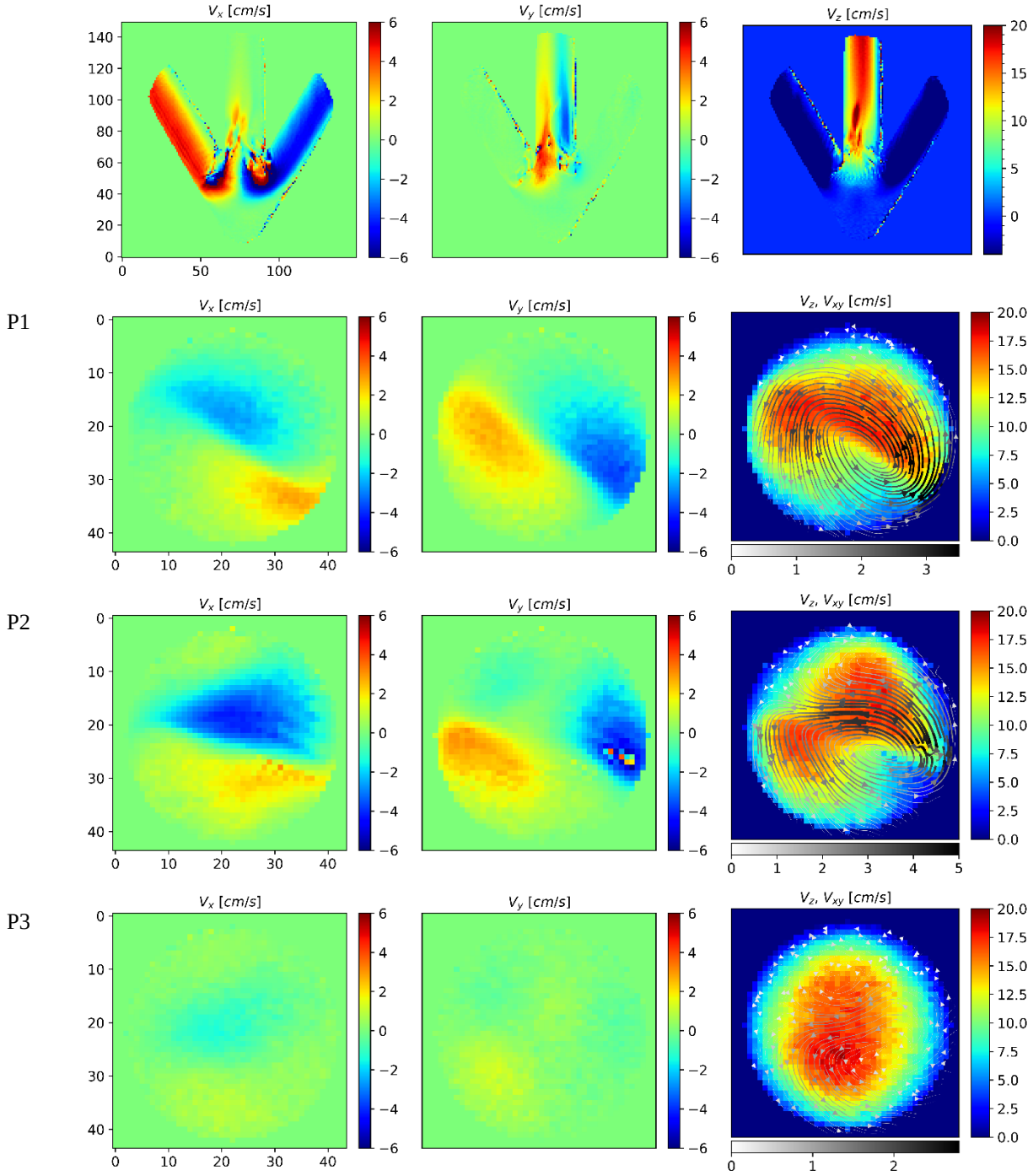

Fig. S13: 3D v*elocity maps obtained with the developed milli-coil. The flow rate on each inlet is 2.4ml/min corresponding to* Re_{outlet} *of 102. The velocity maps in the orthogonal plane to the main flow direction are obtained at slice positions P1, P2 and P3 corresponding respectively to 2mm, 2.5mm and 3mm from the mixing point.*

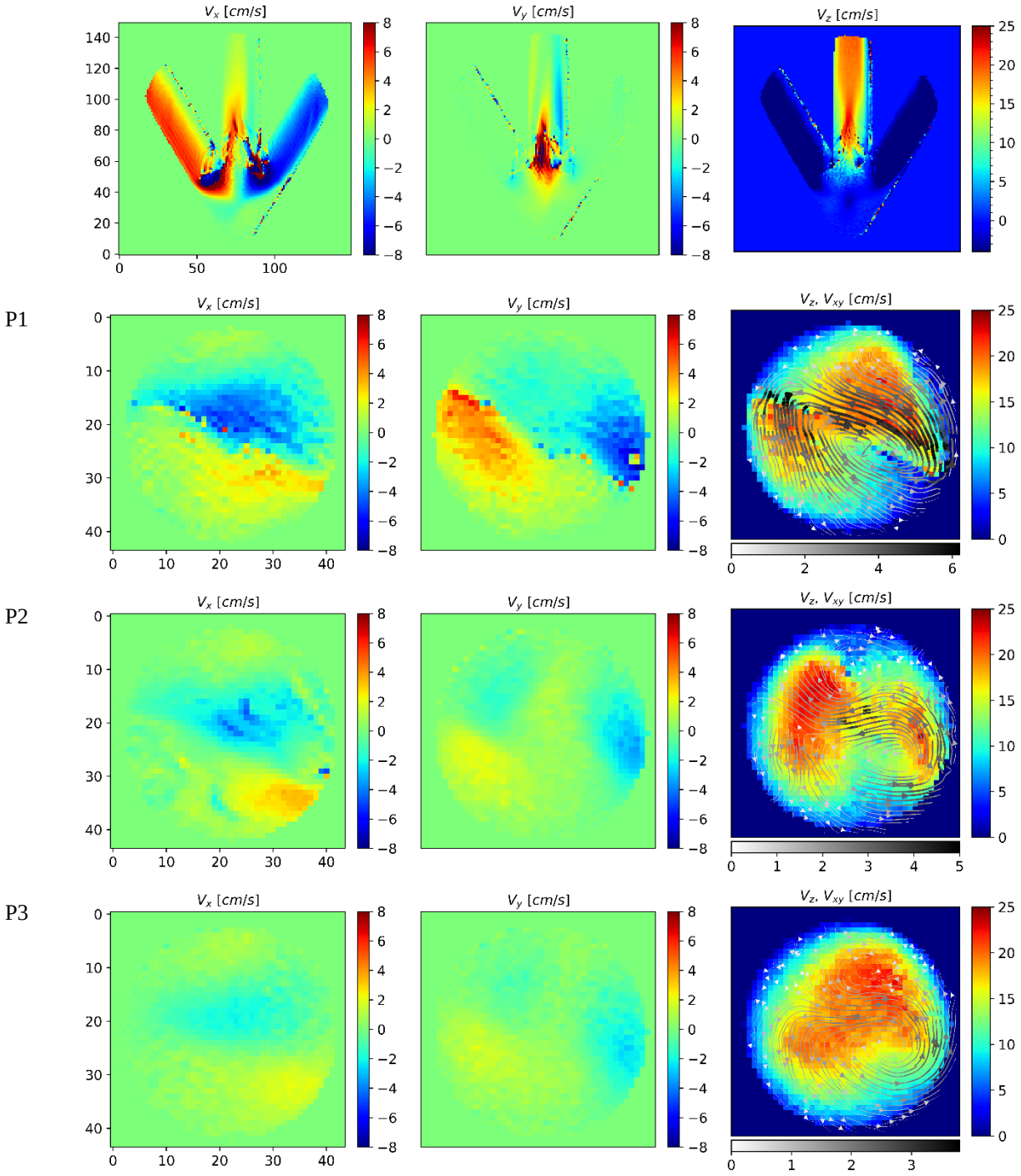

Fig.S14: 3D v*elocity maps obtained with the developed milli-coil. The flow rate on each inlet is 2.9ml/min corresponding to* Re_{outlet} *of 123. The velocity maps in the orthogonal plane to the main flow direction are obtained at slice positions P1, P2 and P3 corresponding respectively to 2mm, 2.5mm and 3mm from the mixing point.*

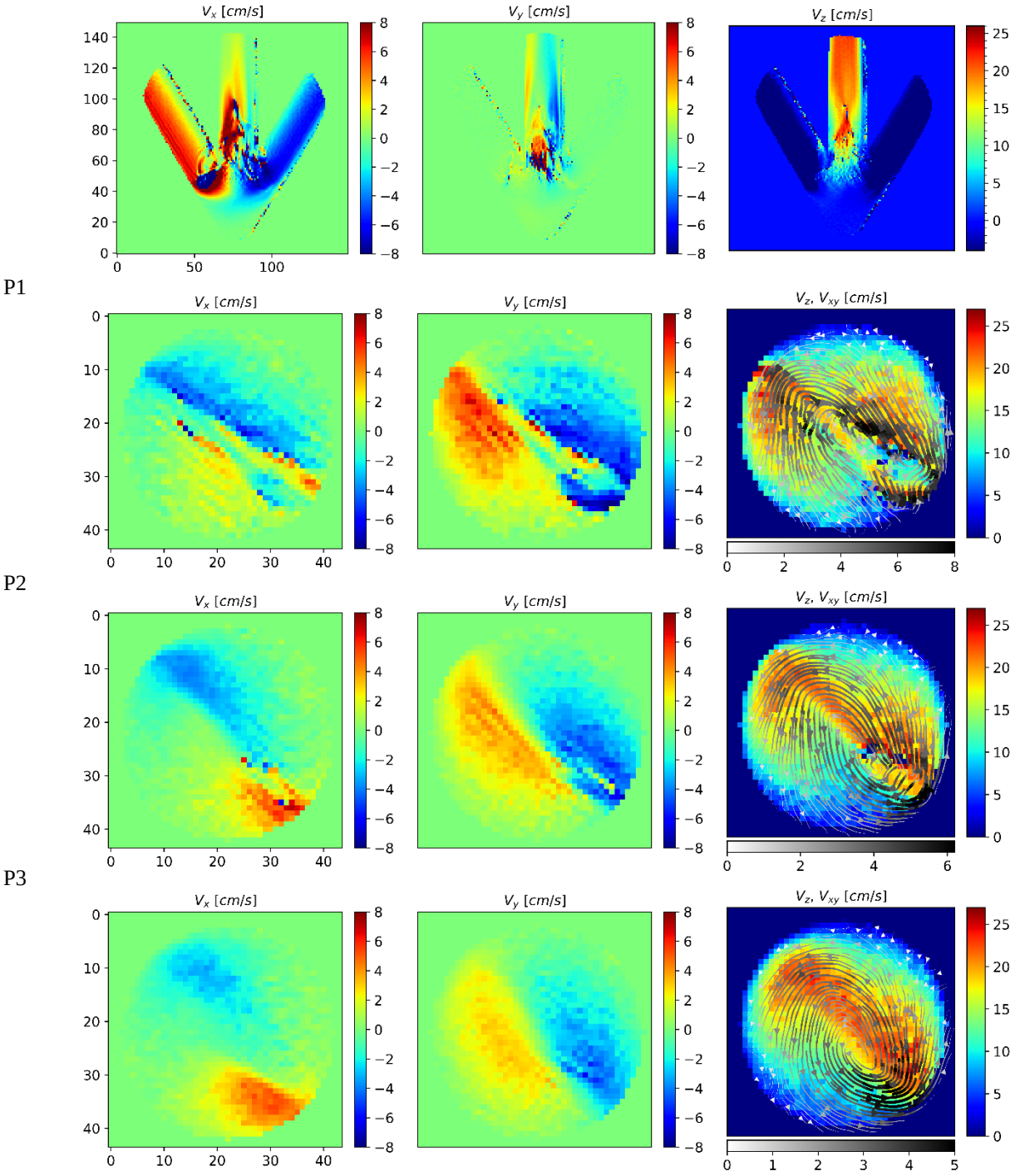

Fig. S15: 3D v*elocity maps obtained with the developed milli-coil. The flow rate on each inlet is 3.2ml/min corresponding to* Re_{outlet} *of 136. The velocity maps in the orthogonal plane to the main flow direction are obtained at slice positions P1, P2 and P3 corresponding respectively to 2mm, 2.5mm and 3mm from the mixing point.*

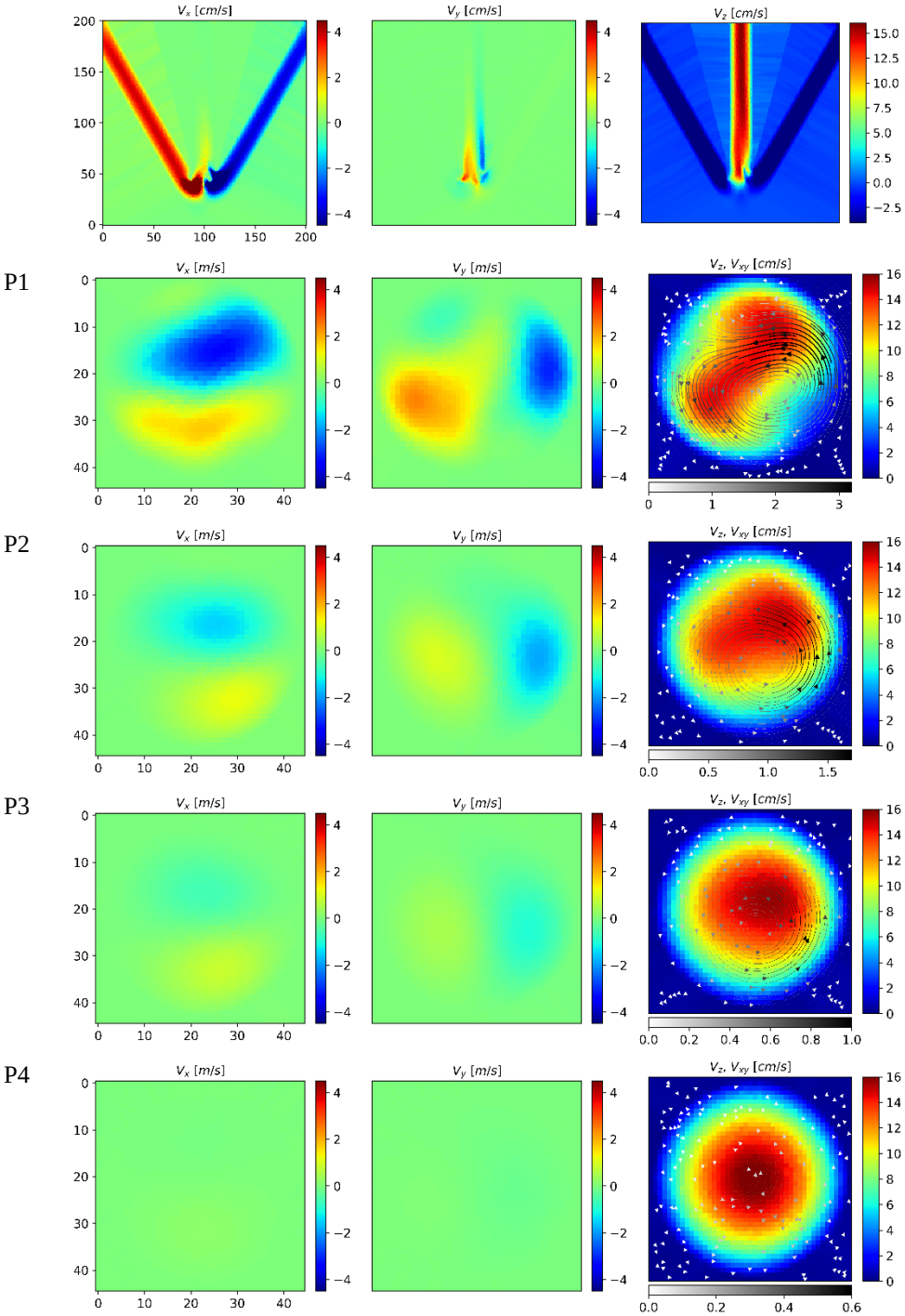

Fig. S16: 3D v*elocity maps obtained with CFD simulation on real geometry of the micromixer. The flow rate on each inlet is 1.9 ml/min corresponding to* Re_{outlet} *of 80. The velocity maps in the orthogonal plane to the main flow direction are obtained at slice positions P1, P2, P3 and P4 corresponding respectively to 2mm, 3mm, 4mm and 7mm from the mixing point.*

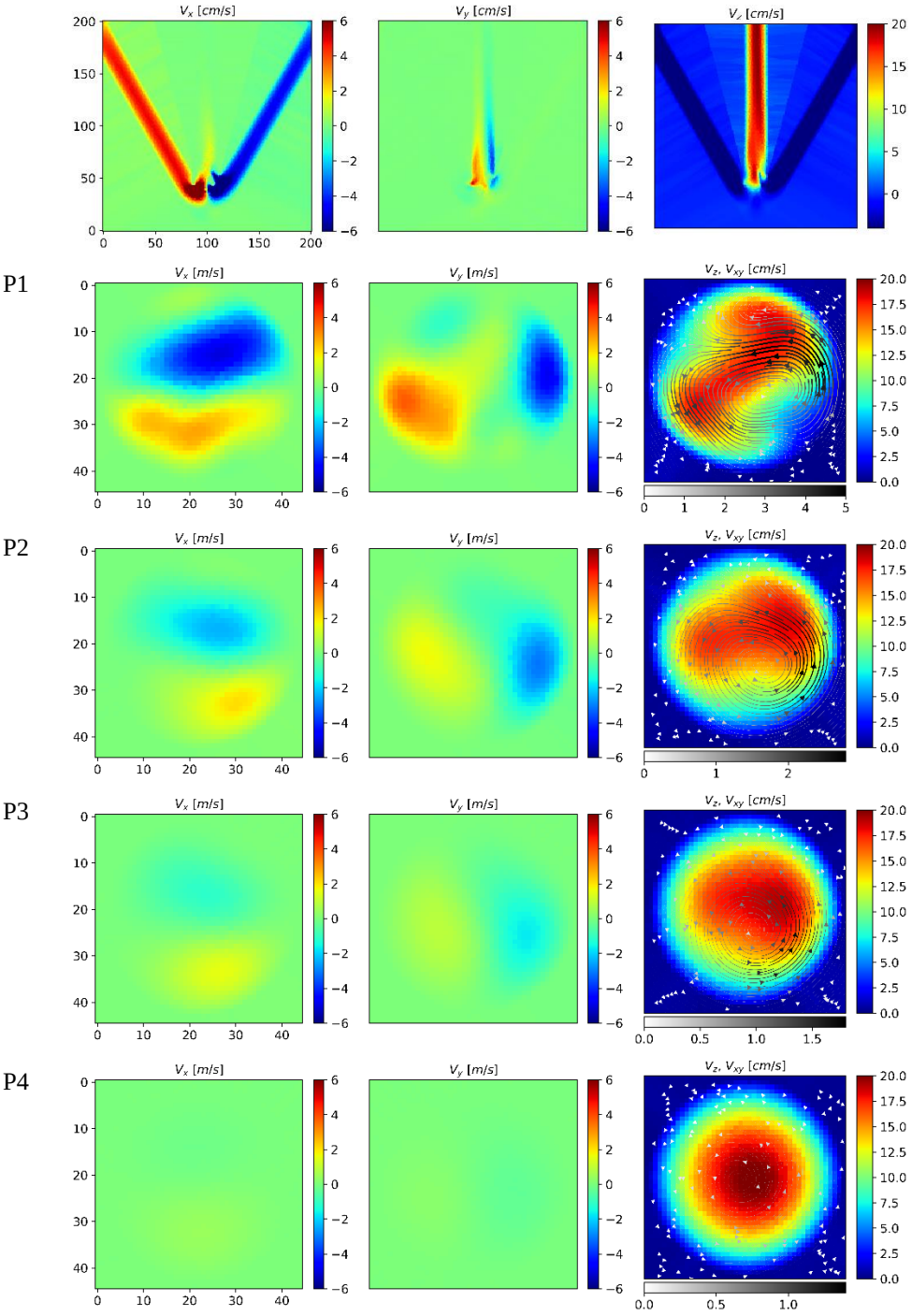

Fig. S17: 3D v*elocity maps obtained with CFD simulation on real geometry of the micromixer. The flow rate on each inlet is 2.4 ml/min corresponding to* Re_{outlet} *of 102. The velocity maps in the orthogonal plane to the main flow direction are obtained at slice positions P1, P2, P3 and P4 corresponding respectively to 2mm, 3mm, 4mm and 7mm from the mixing point.*

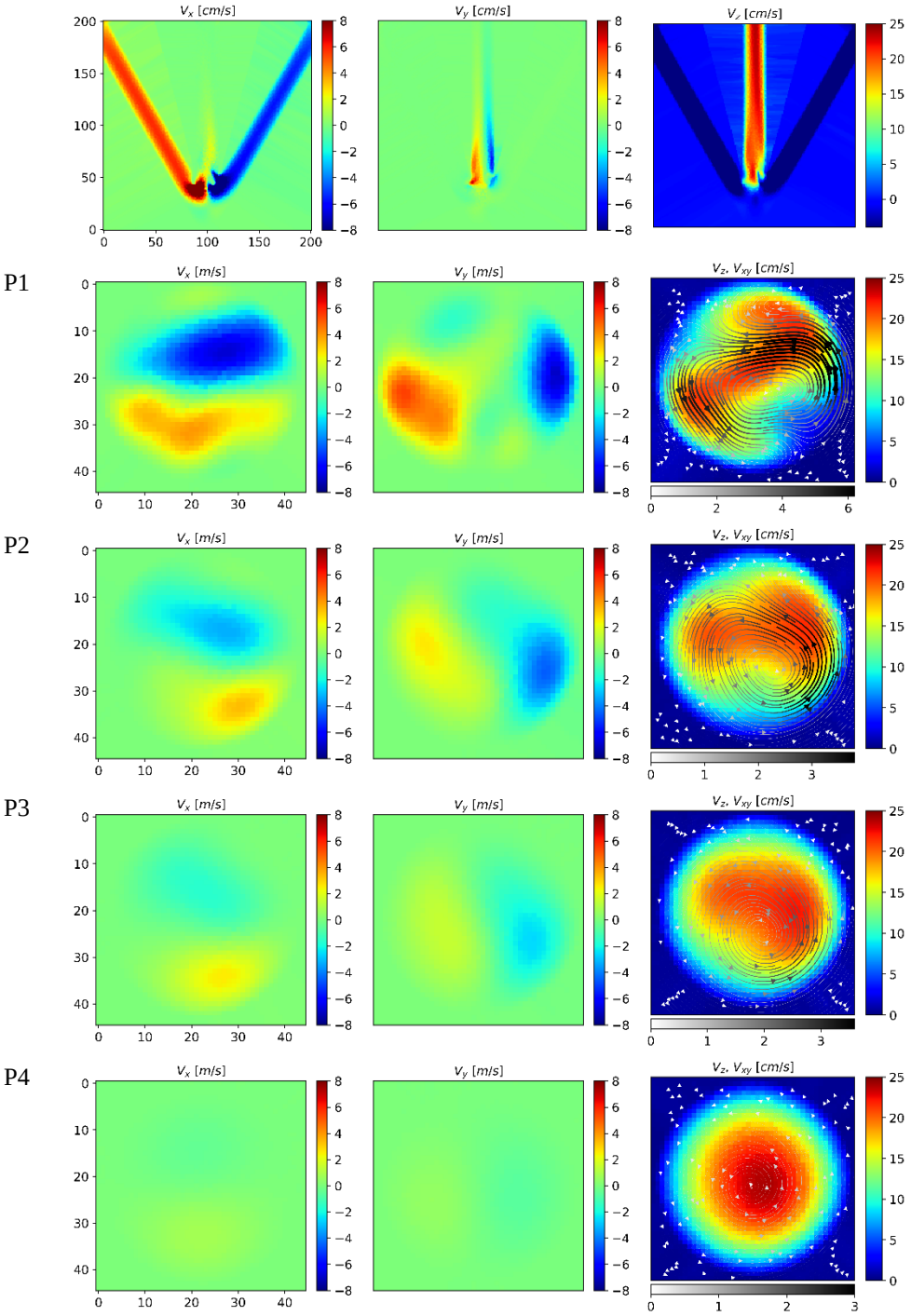

Fig. S18: 3D v*elocity maps obtained with CFD simulation on real geometry of the micromixer. The flow rate on each inlet is 2.9 ml/min corresponding to* Re_{outlet} *of 123. The velocity maps in the orthogonal plane to the main flow direction are obtained at slice positions P1, P2, P3 and P4 corresponding respectively to 2mm, 3mm, 4mm and 7mm from the mixing point.*

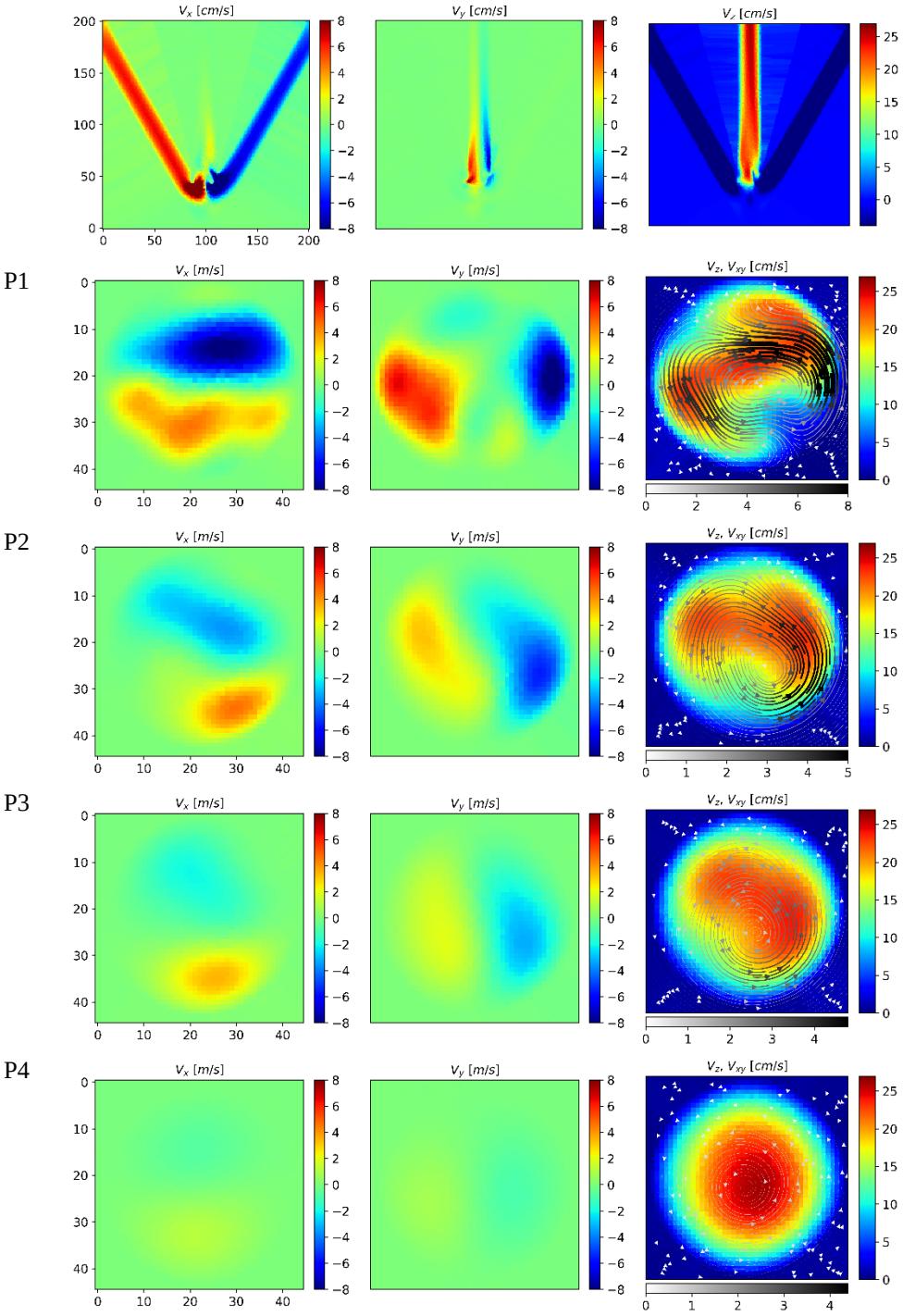

Fig. S19: 3D v*elocity maps obtained with CFD simulation on real geometry of the micromixer. The flow rate on each inlet is 3.2 ml/min corresponding to* Re_{outlet} *of 136. The velocity maps in the orthogonal plane to the main flow direction are obtained at slice positions P1, P2, P3 and P4 corresponding respectively to 2mm, 3mm, 4mm and 7mm from the mixing point.*

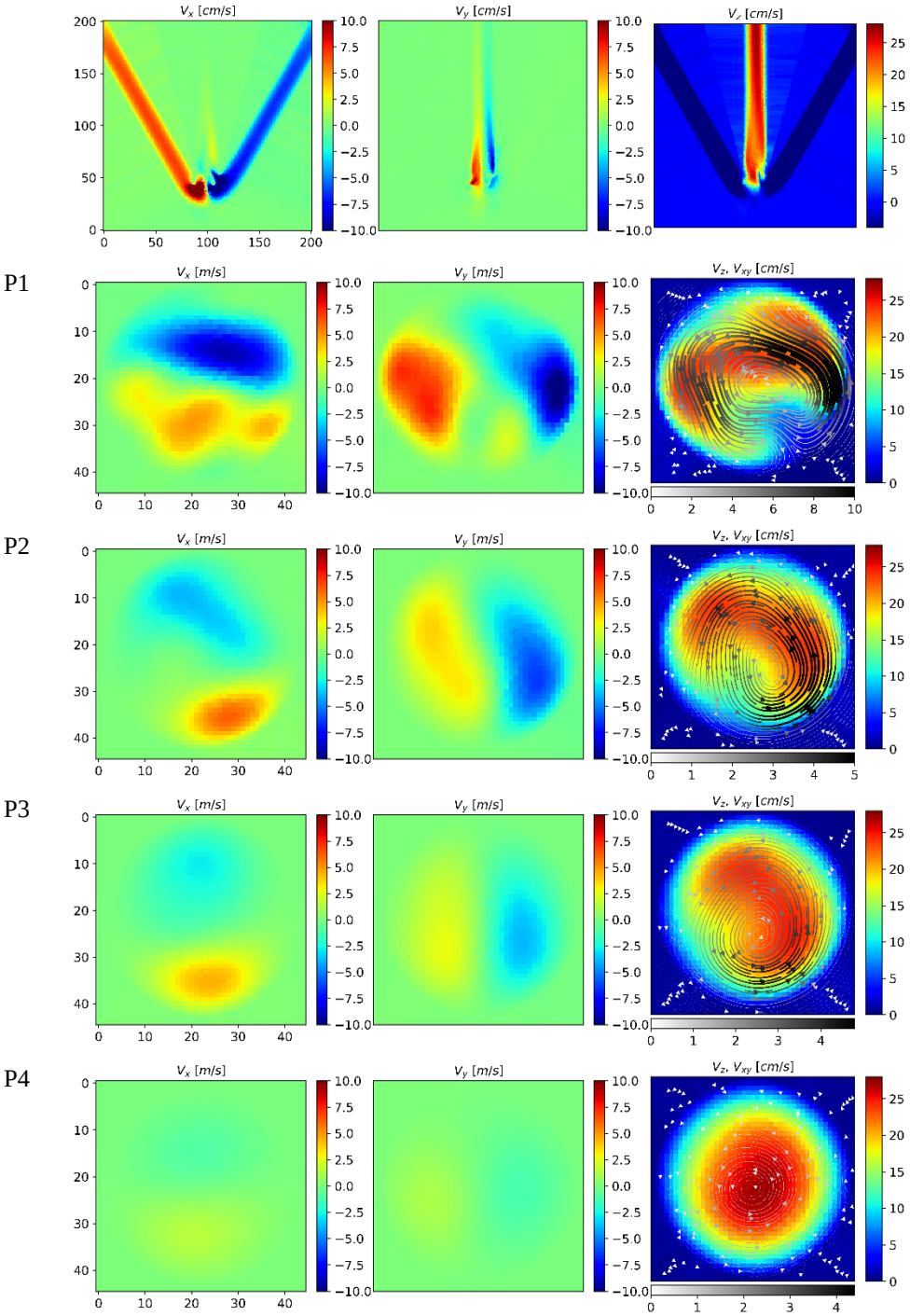

Fig. S20: 3D v*elocity maps obtained with CFD simulation on real geometry of the micromixer. The flow rate on each inlet is 3.4 ml/min corresponding to* Re_{outlet} *of 144. The velocity maps in the orthogonal plane to the main flow direction are obtained at slice positions P1, P2, P3 and P4 corresponding respectively to 2mm, 3mm, 4mm and 7mm from the mixing point.*

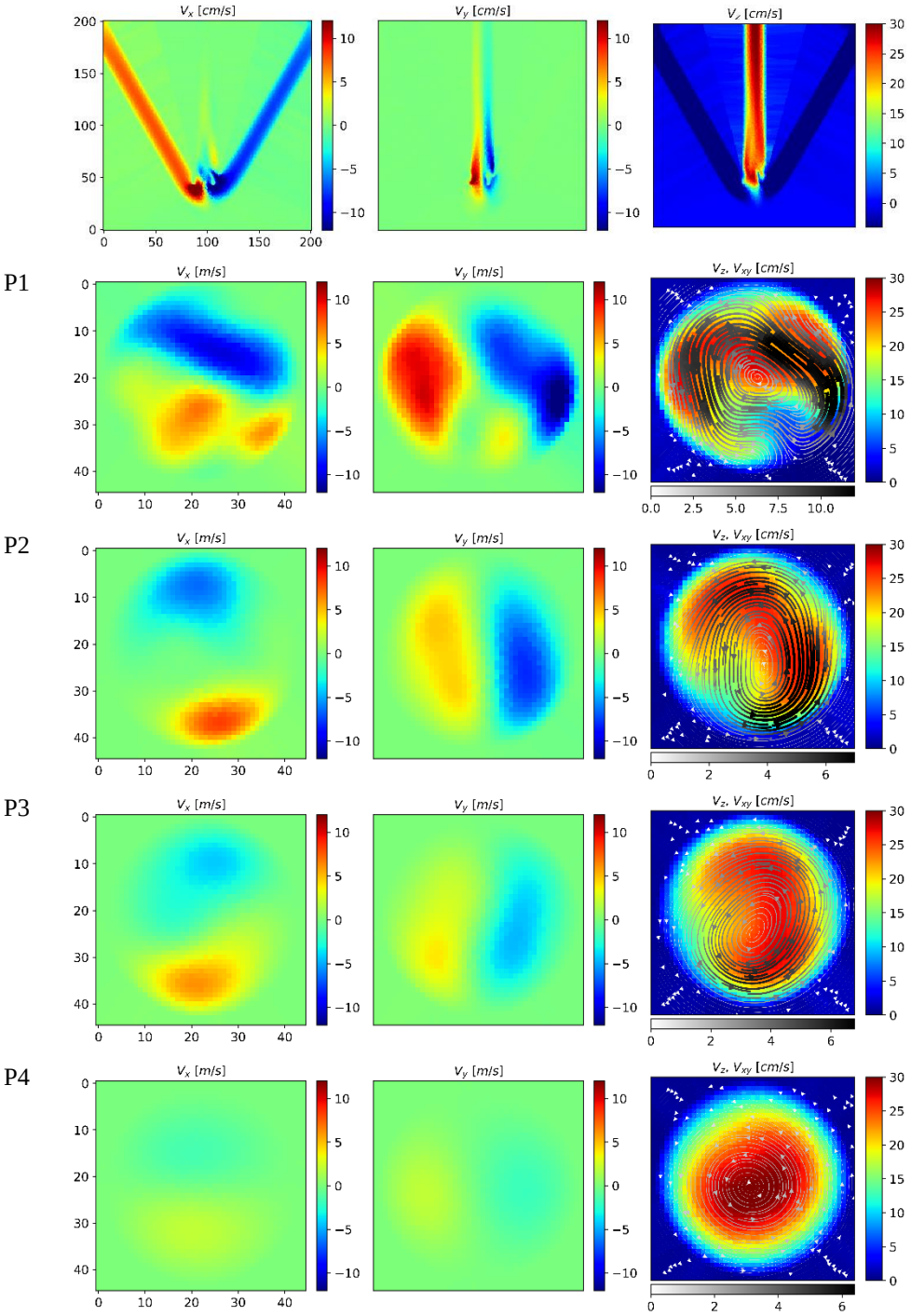

Fig. S21: 3D v*elocity maps obtained with CFD simulation on real geometry of the micromixer. The flow rate on each inlet is 3.9 ml/min corresponding to* Re_{outlet} *of 165. The velocity maps in the orthogonal plane to the main flow direction are obtained at slice positions P1, P2, P3 and P4 corresponding respectively to 2mm, 3mm, 4mm and 7mm from the mixing point.*

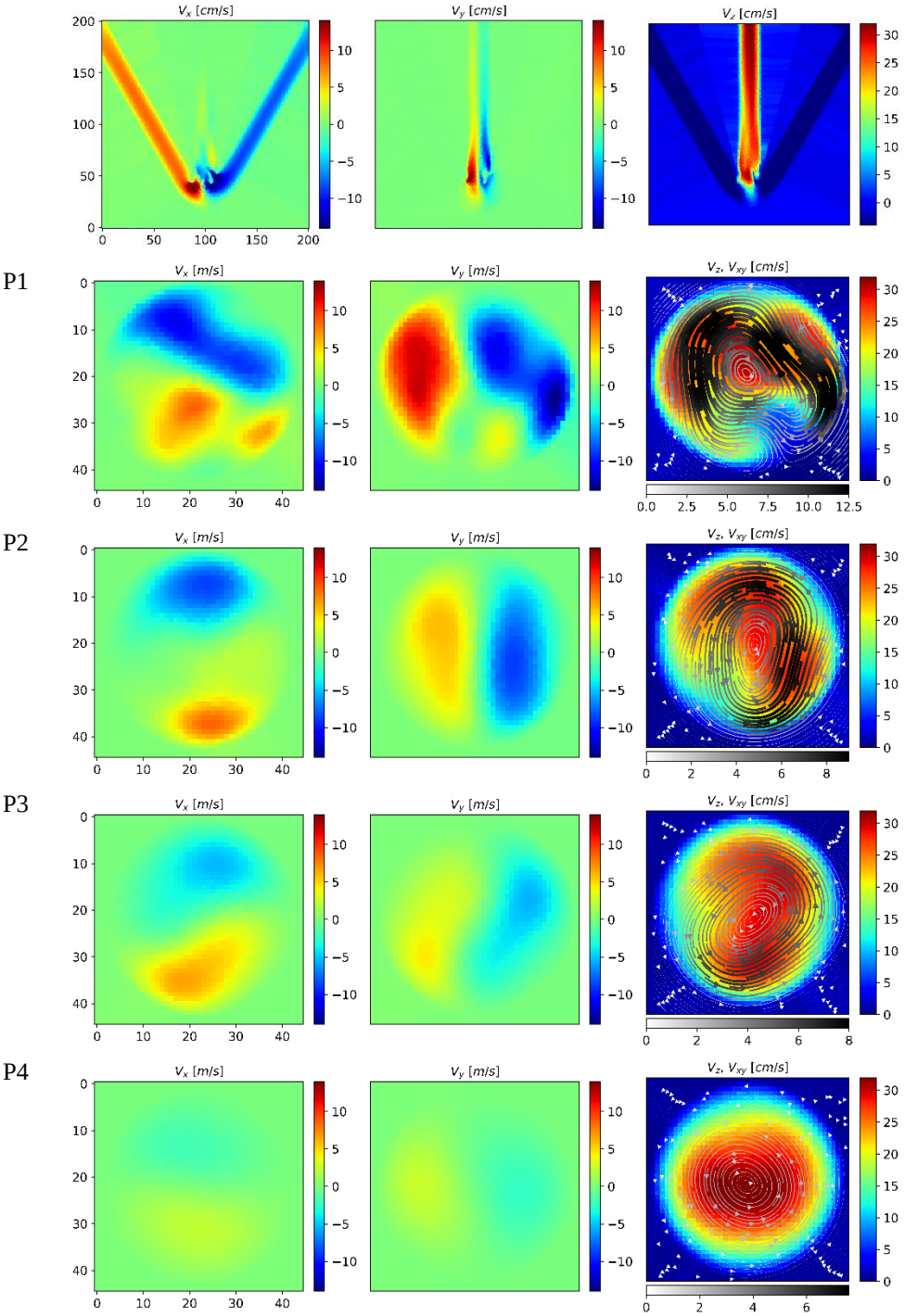

Fig. S22: 3D v*elocity maps obtained with CFD simulation on real geometry of the micromixer. The flow rate on each inlet is 4.2 ml/min corresponding to* Re_{outlet} *of 178. The velocity maps in the orthogonal plane to the main flow direction are obtained at slice positions P1, P2, P3 and P4 corresponding respectively to 2mm, 3mm, 4mm and 7mm from the mixing point.*

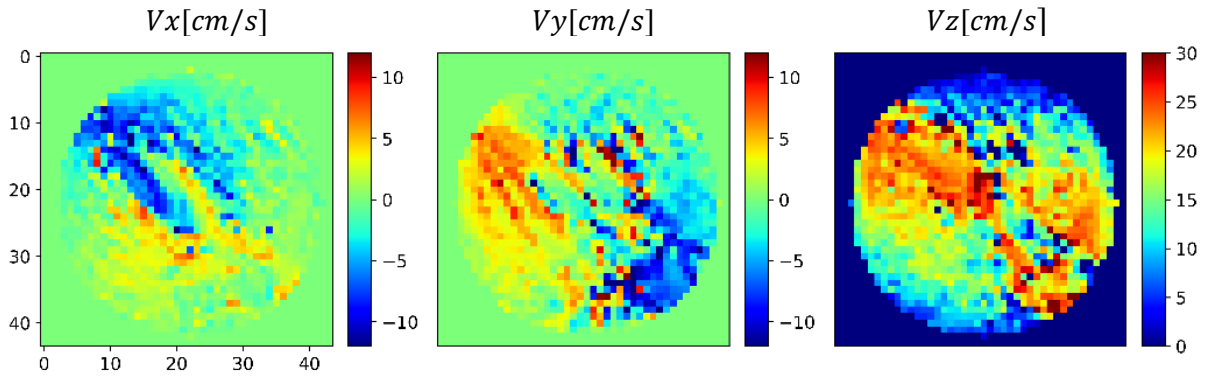

Fig. S23: *3D velocity maps obtained with the developed milli-coil (3.9 ml/min per inlet corresponding to* Re_{outlet} *of 165) illustrating the limit of the MRI measurement*